Decadal Trends in the Oceanic Storage of Anthropogenic Carbon from 1994 to 2014

Jens Daniel Müller[1] (0000-0003-3137-0883), N. Gruber[1] (0000-0002-2085-2310), B. Carter[2,3] (0000-0003-2445-0711), R. Feely[3] (0000-0003-3245-3568), M. Ishii[4] (0000-0002-7328-4599), N. Lange[5], S.K. Lauvset[6] (0000-0001-8498-4067), A. Murata[7] (0000-0002-5931-2784), A. Olsen[8] (0000-0003-1696-9142), F.F. Pérez[9,10] (0000-0003-4836-8974), C. Sabine[12] (0000-0001-6945-8552), T. Tanhua[5] 0000-0002-0313-2557, R. Wanninkhof[13] (0000-0003-1973-3514), D. Zhu[1] (0000-0002-6033-9079)

[1]Environmental Physics, Institute of Biogeochemistry and Pollutant Dynamics, ETH Zurich, Zurich, Switzerland.

[2]Cooperative Institute for Climate, Ocean, and Ecosystem Studies, University of Washington, Seattle, WA, 98105.

[3]Pacific Marine Environmental Laboratory, National Oceanic and Atmospheric Administration, Seattle, WA, 98115.

[4]Meteorological Research Institute, Japan Meteorological Agency, Tsukuba, Japan.

[5]GEOMAR Helmholtz Centre for Ocean Research Kiel, Kiel, Germany.

[6]NORCE Norwegian Research Centre, Bjerknes Centre for Climate Research, Bergen, Norway.

[7]Japan Agency for Marine-Earth Science and Technology, Yokosuka, Kanagawa, 237-0061, Japan.

[8]Geophysical Institute, University of Bergen and Bjerknes Centre for Climate Research, Bergen, Norway.

[9]Instituto de Investigaciones Marinas (IIM), CSIC, Vigo, Spain.

[10]Oceans Department, Stanford University, Stanford, CA 94305, USA.

[12]University of Hawaii at Manoa, Honolulu, HI, 96822.

[13]Atlantic Oceanographic and Meteorological Laboratory, National Oceanographic and Atmospheric Administration, Miami, USA.

[2,3,13]authors with this affiliation are provisionally included on this submission until pending routine institutional review is completed

Corresponding author: Jens Daniel Müller (jensdaniel.mueller@usys.ethz.ch)

31   **Key Points:**

32   ● The global ocean storage of anthropogenic carbon grew by 29 ± 3 and 27 ± 3 Pg C

33   dec^{-1} from 1994 to 2004 and 2004 to 2014, respectively

34   ● The fraction of anthropogenic emissions taken up by the ocean decreased from 36 ± 4

35   to 27 ± 3 % from the first to the second decade

36   ● This reduction is attributed to a decrease of the ocean buffer capacity and changes in

37   ocean circulation

38   **Abstract**

39   The oceanic storage of anthropogenic CO_2 (C_{ant}) that humans have emitted into the

40   atmosphere has been pivotal for counteracting climate change. Yet multi-decadal trends in

41   the ocean interior storage of C_{ant} have not been assessed at global scale. Here, we determine

42   storage changes of C_{ant} by applying the eMLR(C*) regression method to ocean interior

43   observations collected between 1989 and 2020. We find that the global ocean storage of C_{ant}

44   grew by 29 ± 3 Pg C dec^{-1} and 27 ± 3 Pg C dec^{-1} (±1σ) from 1994 to 2004 and 2004 to 2014,

45   respectively. Although the two growth rates are not significantly different, they imply a

46   reduction of the oceanic uptake fraction of the anthropogenic emissions from 36 ± 4 % to 27

47   ± 3 % from the first to the second decade. We attribute this reduction to a decrease of the

48   ocean buffer capacity and changes in ocean circulation. In the Atlantic Ocean, the maximum

49   storage rate shifted from the Northern to the Southern Hemisphere, plausibly caused by a

50   weaker formation rate of North Atlantic Deep Waters and an intensified ventilation of mode

51   and intermediate waters in the Southern Hemisphere. Between 1994 and 2004, the oceanic

52   C_{ant} accumulation exceeded the net air-sea flux by 8 ± 4 Pg C dec^{-1}, suggesting a loss of

53   natural carbon from the ocean during this decade. Our results reveal a substantial sensitivity

54   of the ocean carbon sink to climate variability and change.

55   **Plain language summary**

56   The ocean takes up about 30% of the CO_2 that is emitted to the atmosphere by human

57   (anthropogenic) activities. The removal of this anthropogenic CO_2 from the atmosphere

58   counteracts climate change. The rate at which the ocean takes up anthropogenic CO_2 is

59   controlled by its transport from the surface to the depth of the ocean, where most of it

60   accumulates. Thus, we can quantify and understand the oceanic uptake by keeping track of

61   the accumulation of anthropogenic CO_2 in the ocean interior. In this study, we use a global

60   collection of measurements of CO_2 in seawater to infer the temporal evolution of this

61   accumulation between 1994 and 2014. We find that the ocean continued to act as a strong

62   sink for CO_2 over this period. However, the sink efficiency, which is the uptake per

63   anthropogenic emissions of CO_2, decreased from the first (1994-2004) to the second decade

64   (2004-2014) of our study. Our findings suggest that the ocean sink for CO_2 might further

65   reduce as climate change progresses.

68 **1 Introduction**

69 As a consequence of climate change, the ocean is warming, acidifying, becoming more
70 stratified, and experiencing increasing winds and an intensified hydrological cycle (Cheng et
71 al., 2022; Jiang et al., 2019; Li et al., 2020; Young and Ribal, 2019; IPCC, 2019). While the
72 ocean itself has been vital to mitigate climate change over the past two centuries through its
73 removal of CO_2 from the atmosphere (Gruber et al., in press), a key concern is whether the
74 ocean carbon sink will maintain its function in a changing climate. Models and observation-
75 based estimates agree that since the beginning of the industrial period, the ocean has taken up
76 roughly 30% of the total human CO_2 emissions due to fossil fuel combustion, cement
77 production, and land use change (Friedlingstein et al., 2022; Sabine et al., 2004; Gruber et al.,
78 2019; Khatiwala et al., 2013, 2009). The observations from the first global survey of CO_2 in
79 the ocean interior during the 1980s and 1990s (Wallace, 1995; Key et al., 2004) provided an
80 important pillar for this consensus, demonstrating that between ~1800 and 1994, the ocean
81 had taken up 118 ± 19 petagrams (10^{15}g) of anthropogenic carbon from the atmosphere
82 (Sabine et al., 2004). Anthropogenic carbon (C_{ant}) refers to the additional inorganic carbon
83 present in the ocean-atmosphere system due to human CO_2 emissions to the atmosphere
84 (Gruber et al., in press). We denote temporal changes in the ocean interior content of C_{ant} as
85 ΔC_{ant}.

86 Another pillar supporting the consensus about the strength of the oceanic C_{ant} sink was
87 established when the observational data were extended with the ocean interior measurements
88 gathered during the second cycle of the repeat hydrography program in the framework of
89 GO-SHIP, the Global Ocean Ship-based Hydrographic Investigations Program (Talley et al.,
90 2016). Applying a modified version of the extended Multiple Linear Regression method
91 (eMLR(C*)) to the data available until the early 2010s, Gruber et al. (2019) demonstrated
92 that the ocean took up an additional 34 ± 4 Pg C of C_{ant} from 1994 to 2007 corresponding to a
93 mean decadal storage rate of 26 ± 3 Pg C dec^{-1}. This globally integrated storage rate is
94 indistinguishable from the growth that one would predict from the total C_{ant} storage in 1994
95 and assuming an increase of this inventory proportional with the rise in atmospheric CO_2.
96 Hence, this finding suggested that up to 2007, the globally integrated oceanic C_{ant} sink had
97 been responding in near steady-state fashion to the anthropogenic perturbation, without
98 showing any discernible impact of climate change.

99   However, a first indication of a deviation from this proportional steady-state accumulation
100   emerged in the spatial patterns of the reconstructed changes in C_{ant} storage between 1994 and
101   2007 (Gruber et al., 2019). By comparing these changes with those expected on the basis of
102   the reconstructed storage of C_{ant} for 1994 (Sabine et al., 2004), Gruber et al (2019) found a
103   roughly 20% decrease of the storage rate in the North Atlantic compensated by an increased
104   storage rate in the South Atlantic. However, the robustness of these shifts remains unclear,
105   because they were derived from the comparison of results from two different methodological
106   approaches, both with poorly characterised uncertainties at the regional scale.

107   A second indication of a deviation from the proportional steady-state uptake emerged from
108   the analysis of the difference between the ocean interior storage changes of C_{ant} and the net
109   air-sea fluxes of CO_2 determined based on sea surface observations of pCO_2 (Landschützer et
110   al., 2016). These surface flux estimates include the transfer of both anthropogenic CO_2 and
111   natural CO_2 across the air-sea interface, with the latter referring to the carbon that was
112   already present in the Earth System in preindustrial times (Gruber et al., in press). The
113   difference between storage and net fluxes amounted to 5 ± 3 Pg C over the 1994–2007 period
114   and was interpreted as a non-steady state (i.e., climate-driven) outgassing of natural CO_2 from
115   the ocean.

116   While some studies suggested that the outgassing of natural CO_2 may contribute to a long-
117   term saturation of the oceanic carbon sink (Le Quéré et al., 2007), recent surface flux
118   estimates actually suggest that the net global ocean carbon sink increased strongly over the
119   past decade (Friedlingstein et al., 2022; Fay et al., 2021). But for reasons not yet fully
120   understood, Global Ocean Biogeochemical Models (GOBMs) tend to suggest a smaller
121   increase in uptake since around 2002 compared to the estimates based on the surface ocean
122   pCO_2 observations (Hauck et al., 2019, Friedlingstein et al., 2022). Hence, the discrepancy
123   between these two methods increased over the 2010s, culminating in the surface flux
124   products estimating a 0.6 Pg C yr^{-1} stronger sink than the GOBMs for the 2010s
125   (Friedlingstein et al., 2022). This discrepancy forces the authors of the Global Carbon Budget
126   (GCB) to assign only a medium confidence level to the ocean sink estimate, as it represents
127   the mean of these models and surface flux products (Friedlingstein et al., 2022). Thus,
128   independent information about the oceanic uptake of CO_2 by extending the knowledge about
129   the oceanic accumulation of C_{ant} beyond 2007 would be very useful to help resolving this

130 discrepancy and to better understand the drivers for the changes in the strength of the ocean

131 carbon sink.

132 Some independent information about the evolution of the ocean sink beyond 2007 is already

133 available from regional analyses of the accumulation of C_{ant} over the last few decades. In the

134 Pacific Ocean the C_{ant} inventory change was found to have increased from 8.8 ± 1.1 Pg C dec^{-1}

135 between 1995 and 2005 to 11.7 ± 1.1 Pg C dec^{-1} between 2005 and 2015 (Carter et al.,

136 2019). Even more pronounced increases were reported for the North Atlantic Ocean with an

137 intensification of the C_{ant} storage from 1.9 ± 0.4 Pg C dec^{-1} for the 1989–2003 period to $4.4 \pm$

138 0.9 Pg C dec^{-1} from 2003 to 2014 (Woosley et al., 2016; Wanninkhof et al., 2010). While

139 Woosley et al. (2016) reported a rather steady uptake behaviour in the South Atlantic, Gao et

140 al. (2022) found that the rates of C_{ant} storage accelerated from the 1990s to the 2000s. In all

141 regional studies, the temporal variability of the C_{ant} storage was attributed to changing

142 ventilation patterns of the upper ocean. However, differences in time periods and statistical

143 methods applied in the regional studies limit their synoptic assessment and prevent

144 combining them into a global reconstruction of the oceanic increase in C_{ant} storage since

145 2007.

146 Such an extension of the reconstruction of the global increase in C_{ant} storage beyond 2007 is

147 the key aim of this study. Our work profits from including ~100,000 additional observations

148 of dissolved inorganic carbon (DIC) and related biogeochemical variables collected over the

149 2010s, which were compiled, quality-controlled, and made available by GLODAP, the

150 Global Ocean Data Analysis Project (Lauvset et al., 2021). By consistently determining the

151 storage increase between 1994 and 2004, and between 2004 and 2014, and benefitting from

152 the reconstructed storage of C_{ant} for 1994, we can investigate for the first time the temporal

153 evolution of the global increase in the oceanic storage of C_{ant}. This permits us to address

154 whether the ocean has maintained its vital sink function in a changing climate. Our global-

155 scale reconstruction of the oceanic storage of C_{ant} further serves as an important independent

156 reference point for the ocean carbon sink estimates established by other means, especially in

157 the context of the GCB (Friedlingstein et al., 2022) and the Intergovernmental Panel on

158 Climate Change (IPCC) (Canadell et al., 2021).

2 Material and Methods

2.1 Overview of the Approach

Our global-scale analysis of the changes in the content of C_{ant} (ΔC_{ant}) is based on measurements of the dissolved inorganic carbon (DIC) content and related hydrographical and biogeochemical properties gathered from 1989–2020 and synthesised in the data product GLODAPv2.2021 (Olsen et al., 2016; Lauvset et al., 2021). This data product includes high-quality measurements from reoccupied sections for the purposes of diagnosing long term climate signals such as the accumulation of C_{ant}. The majority of the data used in this study stem from the JGOFS/WOCE global CO_2 survey conducted in the 1980s and 1990s (Wallace, 1995; Key et al., 2004), the repeat hydrography program GO-SHIP that began in 2003 and is now completing its second cycle (Talley et al., 2016; Sloyan et al., 2019), as well as a number of additional programs, including INDIGO, SAVE, TTO, JOIS, and GEOSECS (Key et al., 2004, and references therein). In addition to DIC, our analysis requires observations of salinity (S), temperature (T), total alkalinity (TA), oxygen (O_2), the apparent oxygen utilisation (AOU), silicate ($Si(OH)_4$), nitrate (NO_3^-), and phosphate (PO_4^{3-}). To extract the ΔC_{ant} signal from these data, we use the eMLR(C*) method (Gruber et al., 2019; Clement and Gruber, 2018) with a few modifications (see details below and in supplement S2).

Our application of the eMLR(C*) method employs the following steps:

1. The semi-conservative tracer C* (Gruber et al., 1996) is calculated from DIC as C* = DIC − 117×[PO_4^{3-}] − 0.5×(TA + 16×[PO_4^{3-}]).

2. The observations are clustered in neutral density slabs and ocean regions (Fig. S1), and assigned to one of the three sampling periods 1989–1999, 2000–2009, or 2010–2020 (Fig. 1).

3. Within each sampling period, the observed C* is adjusted to the respective reference year (t_{ref}) 1994, 2004, or 2014 assuming a transient steady state increase of C_{ant} (Gammon et al., 1982).

4. Within each neutral density slab and ocean region, a set of multiple linear regression (MLR) models are fitted with C*(t_{ref}) as target variable and all possible combinations of at least 2 out of the 7 considered predictor variables S, T, O_2, AOU, $Si(OH)_4$, NO_3^-, PO_4^{3-}.

5. The 10 best common MLR models for two compared sampling periods are selected

190   within each density slab and ocean region based on the summed root mean squared

191   error (RMSE), after excluding MLRs with strong multicollinearity between the

192   predictors (see supplement S2.2).

193   6. The decadal change in anthropogenic carbon is computed as the difference between

194   the average C* distribution for each sampling period, i.e. $\Delta C_{ant} = C^*(t_{ref,n+1},) - C^*(t_{ref,n})$,

195   where the C* distributions are predicted ("mapped") for each t_{ref} by applying the

196   selected MLRs to a common set of predictor climatologies.

197   7. In surface waters, ΔC_{ant} is predicted based on an transient equilibrium approach

198   (McNeil et al., 2003), which assumes that the increase of the surface ocean pCO_2

199   follows that of the atmosphere closely. This approach aims to avoid biases introduced

200   by the seasonal and interannual variability of C* and the predictor variables.

201   The most important differences we introduced relative to the methods described by Clement

202   and Gruber (2018) and Gruber et al. (2019) are detailed in section 2.3 and include a more

203   thorough selection of the predictor variables and MLR models, a more robust and

204   standardised quantification of uncertainties, and an assessment of structural reconstruction

205   uncertainties through tests with synthetic data, which were performed in parallel to the

206   analysis of the real-world observations. Our reconstruction of ΔC_{ant} with the eMLR(C*)

207   method involves a number of choices regarding the configuration of the method. In sections

208   2.2 and 2.3 we describe the standard configuration that we use to derive the results we report

209   as our best informed estimates. In section 2.4, we describe a number of reasonable alternative

210   configurations. We use the offsets between results obtained with these plausible alternatives

211   and the standard configuration as a basis for determining the uncertainty.

212   **2.2 Data**

213   This study relies on ocean interior observations of DIC, TA, S, T, O_2, $Si(OH)_4$, NO_3^-, and

214   PO_4^{3-} collected in the global ocean from 1989 through 2020 (Fig. 1) and provided through

215   GLODAPv2.2021 (Olsen et al., 2016; Lauvset et al., 2021). The apparent oxygen utilisation

216   was calculated from oxygen, salinity, and conservative temperature (Graham and McDougall,

217   2013) according to the solubility from Weiss (1970) and used as an additional predictor

218   variable. Observations were filtered based on the GLODAP flagging scheme, using only

219   highest-quality data identified as those with a f-flag value of 2, which indicates acceptable,

220   measured data according to a simplified version of the WOCE flagging scheme, and a qc-flag

221   value of 1, which indicates adjusted or unadjusted data that have undergone GLODAP's full

222   secondary quality control. With a few exceptions, only samples were included for which all

223   required variables fulfil the strictest quality criteria. We deviated from this only for cases

224   where our tests of the eMLR(C*) method with synthetic data (see supplement S4) revealed

225   that omitting observations because of only one missing variable increased the biases of the

226   ΔC_{ant} reconstructions. In these cases either data that did not fulfil the strictest quality criteria

227   were included (7609 samples, 3.7% of all samples), or missing data were filled (7305

228   samples, 3.5%) using CANYON-B (Bittig et al., 2018) predictions (see supplement S1.3). In

229   total, we used 206'836 samples for our standard case reconstruction.
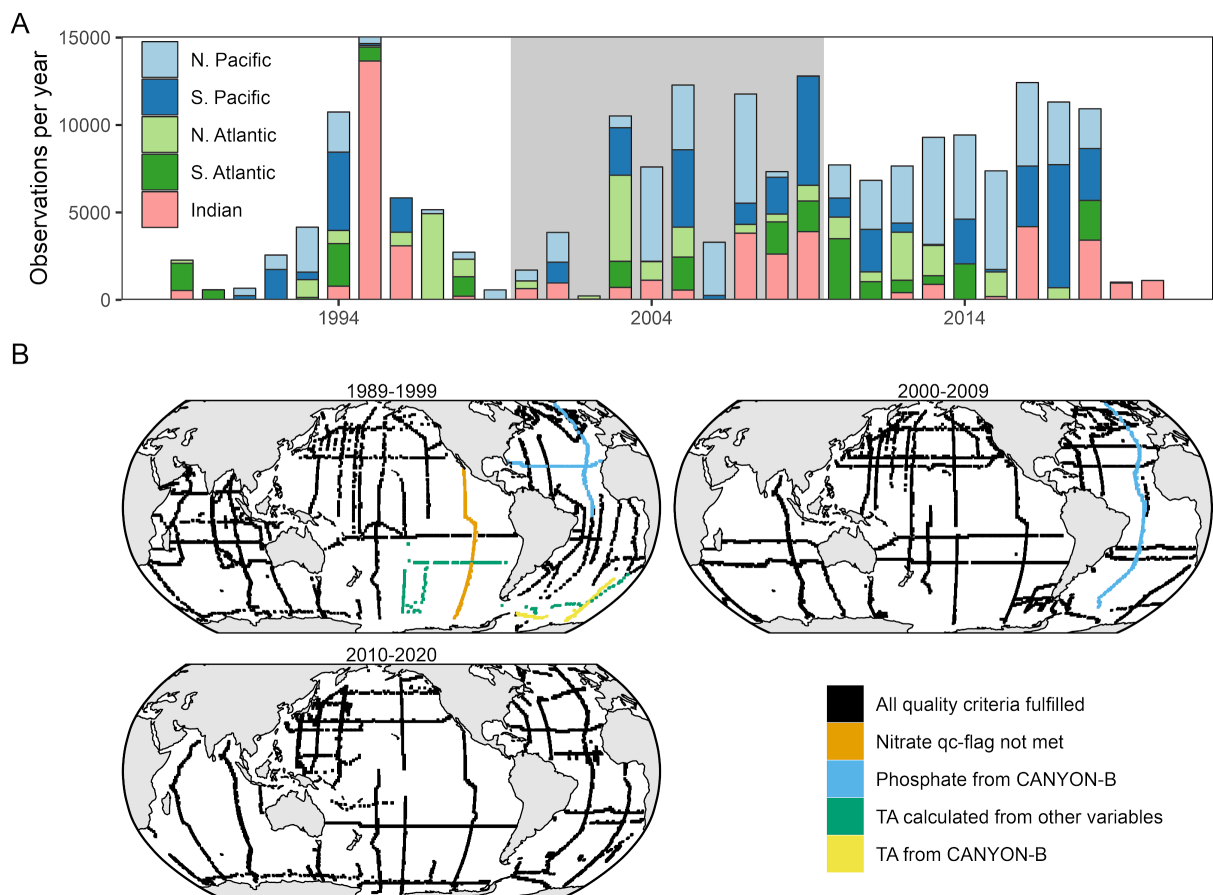
230   **Fig. 1**: Spatio-temporal coverage of observations from 1989–2020 as provided through

231   GLODAPv2.2021 and after applying our flagging criteria. (A) Number of observations per year,

232   where colours distinguish sampling regions according to the basin mask definition "5" in Fig. S1. The

233   shaded background indicates the assigned sampling periods 1989–1999 ($t_{ref,1}$ = 1994), 2000–2009 ($t_{ref,2}$

234   = 2004), and 2010–2020 ($t_{ref,3}$ = 2014). (B) Map of observations as used in our standard case for the

235   three sampling periods. Cruises that fulfilled all flagging criteria are displayed in black, while cruises

236   for which one parameter did not fulfil all criteria but were still included (see also Table S1) are

237   highlighted in colour.

238   Although the GLODAP data have already undergone a secondary quality control and are —
239   if required — adjusted to improve their internal consistency, we applied a number of
240   additional adjustments to the DIC, TA, and phosphate observations, based either on our
241   decade-by-decade reanalysis of deep water crossovers originally determined by GLODAP, or
242   on previously unaccounted offsets in the measurements of certified reference materials
243   (CRM) for DIC and TA (see supplement S1.2 for details). This affected the majority of the
244   DIC and TA measurements from the Indian Ocean in the 1990s (12843 samples, 6.2% of all
245   samples), and the DIC, TA, and phosphate measurements in the North Pacific from the 2010s
246   (35395 samples, 17.2% of all samples). Our adjustments of the Indian Ocean data have been
247   formally accepted by GLODAP and were applied in the release of GLODAPv2.2022
248   (Lauvset et al., 2022). The magnitude of these additional adjustments are generally small (<2
249   µmol kg^{-1} for DIC, <4 µmol kg^{-1} for TA, and <1% for phosphate) and below the adjustment
250   limits normally considered by GLODAP. Still, these adjustments proved to be critical in our
251   work, since an offset of 1 µmol kg^{-1} in DIC integrated over 3000 m amounts to a column
252   inventory offset of ~3 mol m^{-2}, which is of similar magnitude as some of the decadal changes
253   we are aiming to detect.

254   For the purpose of predicting the C* distributions, we used the objectively analysed
255   climatology for the 1981 – 2010 period for salinity and temperature from the World Ocean
256   Atlas 2018 (Zweng et al., 2019; Locarnini et al., 2019), in combination with phosphate,
257   nitrate, silicate and oxygen from the global interior ocean mapped climatology based on
258   GLODAPv2 (Lauvset et al., 2016). The climatological distribution of AOU was calculated in
259   accordance with the observational data.

260   **2.3 Standard configuration of the eMLR(C*) method**

261   In the following, we describe the main changes of the eMLR(C*) method in comparison to
262   the previous analysis by Gruber et al. (2019). Further minor configuration changes are
263   presented in supplement S2.

264   **2.3.1 Temporal clustering and C* adjustment to reference year**

265   For the temporal clustering of the data, we assigned each observation to one of the following
266   three sampling periods (start and end years included):

267   1989–1999 ($t_{ref,1}$ = 1994)

268   2000–2009 ($t_{ref,2}$ = 2004)

269   2010–2020 ($t_{ref,3}$ = 2014)

270   with the assigned reference years (t_{ref}) given in parenthesis.

271   Based on these three sampling periods, we estimated the C_{ant} storage changes between the
272   reference years 1994–2004 and 2004–2014 (Fig. 1). The ΔC_{ant} estimates represent the
273   changes over exactly ten years, from mid-year of the first to mid-year of the second reference
274   year. In addition, we determined ΔC_{ant} directly for the twenty year period 1994–2014.

275   The adjustment of C* from the time of sample collection (t) to the reference year (t_{ref}) was
276   calculated as $C^*(t_{ref}) = C^*(t) - \delta(t) * C_{ant}(t_{ref})$, with $\delta(t) = \Delta CO_{2,atm}(t-t_{ref}) / \Delta CO_{2,atm}(t_{ref}-t_{pi})$,
277   where t_{pi} indicates preindustrial times (~1800). We estimated the C_{ant} content in the reference
278   year ($C_{ant}(t_{ref})$), by adding a proportional fraction of the reconstructed increase in C_{ant} over 13
279   years between 1994–2007 (ΔC_{ant}(1994–2007), Gruber et al., 2019) to the reconstructed C_{ant} in
280   1994 (C_{ant}(1994)), i.e., ΔC_{ant}(1994–t_{ref}) = (t_{ref}-1994) * ΔC_{ant}(1994–2007) / 13 years.

281   2.3.2 Spatial clustering and subsetting

282   For the fitting of the MLR models and mapping of ΔC_{ant} in the standard configuration, we
283   clustered the observations and predictor climatologies horizontally into the Atlantic, Pacific
284   and Indian Ocean, according to mask "3" of our basin mask definitions (Fig. S1). To assess
285   the contribution of the impact of this choice on the uncertainty of the reconstructed changes
286   in C_{ant}, we investigated five other basin configurations (Fig. S1). For clustering in the vertical
287   dimension, we used the same neutral density levels as employed by Gruber et al. (2019).
288   Surface water samples collected shallower than 100 m were excluded from the MLR fitting to
289   avoid seasonally biased observations.

290   2.3.3 Mapping C* and ΔC_{ant}

291   The spatial distribution of C* was mapped by using the best MLR models of each reference
292   year with climatological distributions of the predictor variables. For this purpose, the ten best
293   MLR models within each spatial cluster were selected as those with the lowest summed
294   RMSE for the two paired sampling periods following Clement and Gruber (2018). The ten
295   individually mapped C* distributions were then averaged and subtracted to derive the mean

296   ΔC_{ant} distribution. In contrast to prior applications of the method, we included negative

297   mapped ΔC_{ant} values, since (i) ΔC_{ant} can regionally be negative when water with low C_{ant}

298   displaces water with high C_{ant}, (ii) setting negative values to zero could lead to positively

299   biased ΔC_{ant} inventories, and (iii) our tests with synthetic data revealed a tendency to lower

300   biases when negative values were retained.

301   **2.3.4 Surface equilibrium ΔC_{ant}**

302   In the standard configuration, the equilibrium ΔC_{ant} distribution at the sea surface was

303   computed based on a rearranged definition of the Revelle factor, γ, as $\Delta C_{ant,eq}(t_{ref,n}-t_{ref,n+1}) = 1/\gamma$

304   $\times$ DIC/pCO$_2$ $\times$ $\Delta pCO_{2,atm}(t_{ref,n+1}-t_{ref,n})$, where DIC, pCO$_2$ and γ are the climatological surface

305   values (Lauvset et al., 2016) adjusted to the mean pCO$_{2,atm}$ of each analysis period. This

306   adjustment of the climatological surface CO$_2$-system parameters to the mean pCO$_{2,atm}$ was

307   achieved by calculating as a first step the surface pCO$_2$ in 2002 based on the climatological

308   values for temperature, salinity, DIC and TA, which are normalised to the same year (Lauvset

309   et al., 2016). In a second step, the surface ocean pCO$_2$ was shifted according to the change in

310   pCO$_{2,atm}$, and DIC and γ were recalculated based on the new surface pCO$_2$. Thus, our surface

311   equilibrium approach takes changes in the surface ocean buffer capacity into consideration.

312   All CO$_2$-system calculations were done with the R-package seacarb (Gattuso et al., 2021)

313   using the CO$_2$ dissociation constants from Lueker et al. (2000), the fluoride association

314   constant from Perez and Fraga (1987) or Dickson & Riley (1979) at temperatures below 9°C

315   and the acidity constant of hydrogen sulphide from Dickson (1990). To assess the

316   uncertainties associated with this equilibrium ΔC_{ant} estimate, we also used an independent

317   observation-based estimate of the increase in surface DIC (Gregor and Gruber, 2021).

318   While previous studies defined a distinct depth and neutral density threshold to separate

319   water masses for which the surface equilibrium or eMLR(C*) reconstructions are used to

320   determine ΔC_{ant}, we blend both estimates smoothly over the top 200 m. For this purpose, the

321   equilibrium ΔC_{ant} is calculated at the sea surface only, while the eMLR-based ΔC_{ant} is initially

322   mapped across the entire water column. In a post processing step, the surface- and eMLR-

323   based ΔC_{ant} estimates are averaged proportionally according to the water depth across the

324   upper 200 m (e.g., 75% surface-based and 25% eMLR(C*)-based estimate at 50 m water

325   depth).

326   **2.4 Computation of global ΔC_{ant} inventories**

327   Column inventories and inventories of ΔC_{ant} in this study represent integrals across the upper

328   3000 m of the water column. ΔC_{ant} reconstructions below 3000 m are not included in integrals

329   to avoid the imprint of ΔC_{ant} uncertainties that are small in terms of amount content but

330   considerable in terms of integrated inventory changes. Instead, we follow previous studies

331   and account for C_{ant} storage changes below 3000 m by adding 2% to our global ΔC_{ant}

332   inventories. This deep ocean scaling represents the fraction of the total C_{ant} inventory in 1994

333   beneath 3000 m according to Sabine et al. (2004). We further scale our global inventories for

334   the storage of C_{ant} in unmapped regions according to previously determined fractions of the

335   global C_{ant} storage that occurs in these regions, namely 2% in the Arctic Ocean (Tanhua et al.,

336   2009), 1.5% in the Mediterranean Sea (Palmiéri et al., 2015), 1% in the Nordic Seas (Olsen et

337   al., 2010), and 0.3% in the Sea of Japan (Park et al., 2006). In sum, the upscaling amounts to

338   7% of our directly mapped global ΔC_{ant} inventory. Regional inventories refer to the integral

339   of directly mapped ΔC_{ant} distributions and no areal scaling was applied, e.g., the regional

340   inventory of the Atlantic Ocean does not account for storage in the Mediterranean Sea. Thus,

341   our global inventory differs from the sum of the regional inventories by 7%.

342   **2.5 Determination of uncertainty and method testing**

343   The primary sources of uncertainty in the eMLR(C*) reconstructions of ΔC_{ant} are structural in

344   nature and involve choices associated with the configuration of the method (Clement and

345   Gruber, 2018, Gruber et al., 2019). According to our assessment, this involves primarily six

346   configuration choices about (1) the regional clustering of the data, (2) the approach to

347   perform data adjustments, (3) the nutrient used to compute the target variable C*, (4) the

348   approach to estimate surface ocean ΔC_{ant}, (5) the gap-filling of flagged data, and (6) the

349   choice of predictor climatologies. In addition, we consider (7) an uncertainty contribution in

350   our global ΔC_{ant} inventories arising from the scaling to account for C_{ant} storage changes in

351   unmapped waters.

352   To assess the impact of these choices and to obtain an estimate of uncertainty of our

353   reconstructions, we have reconstructed a set of total 10 alternative estimates of ΔC_{ant} using

354   modified choices for each of the six configurations listed above. These modifications of the

355   eMLR(C*) configuration are described in detail in supplement S4. We base our estimate of

356   uncertainty on the ΔC_{ant} offsets between the standard case and the reconstructions obtained

357 with the configuration changes. The individual offsets are considered as independent

358 uncertainty contributions and combined as the square root of the sum of the squares (RSS) to

359 derive the standard uncertainty ($\pm 1\sigma$) of our reconstructions, which we consider as a 68%

360 confidence interval. Throughout the results and discussion, we report all results together with

361 this $\pm 1\sigma$ uncertainty. In figures, we display also the expanded $\pm 2\sigma$ uncertainty representing

362 a confidence interval of 95%. For each variable that is derived from a primary ΔC_{ant} estimate

363 (e.g., the decadal difference between two ΔC_{ant} estimates, the ocean-borne fraction, etc.) we

364 combine individual uncertainties through standard error propagation.

365 In order to independently assess the quality of our ΔC_{ant} reconstructions against a known

366 truth, we use synthetic data generated from the global ocean biogeochemical model (GOBM)

367 CESM-ETHZ (Doney et al., 2009; Hauck et al., 2020). The GOBM is a hindcast model

368 forced with reanalysed atmospheric data and the observed atmospheric CO_2 trajectory. The

369 synthetic data set is generated by subsetting the model output in space and time according to

370 availability of real-world observations. The eMLR(C*) approach is then applied to the

371 synthetic data set to reconstruct ΔC_{ant}. The comparison of the reconstructed ΔC_{ant} to the

372 known model truth allows us to determine the biases of the reconstruction in terms of global

373 or regional inventories, column inventory maps, or zonal mean sections. Details and results of

374 this assessment are given in the supplement S5.

375 In order to assess the sensitivity of our reconstructions to other sources of uncertainty, such as

376 the limited sampling of the spatio-temporal variability of the changes in DIC, we performed

377 additional eMLR(C*) analyses, wherein we pushed the configurations beyond the limits of

378 what we consider a reasonable modification. For example, we limited the observations to

379 those from repeatedly occupied sections, used other DIC variants than C* as target variable

380 and omitted any data adjustments (see section 4.2).

3 Results

3.1 Column inventories

383 The storage changes in anthropogenic carbon (ΔC_{ant}) integrated over the upper 3000 m

384 (referred to as column inventories) reveal strong similarities during both decades of our

385 analysis, i.e., between 1994 and 2004, and between 2004 and 2014 (Fig. 2A,B). The ΔC_{ant}

386   column inventories vary markedly with latitude. The highest mean decadal C_{ant} storage

387   changes of about 10 mol m^{-2} dec^{-1} located near the centre of the subtropical gyres (30–40°

388   N/S) are about twice as high as those in the equatorial regions (10° N/S) and in the Southern

389   Ocean south of 60°S. In the Southern Hemisphere, the consistently high ΔC_{ant} column

390   inventories in all subtropical gyres form a circumpolar band, while in the Northern

391   Hemisphere the storage changes per unit area in the Atlantic exceed those in the Pacific

392   roughly by a factor of two. The general patterns of our ΔC_{ant} reconstructions are reminiscent

393   of those reconstructed for the pre-industrial to 1994 period (Sabine et al., 2004) and for the

394   1994 to 2007 period (Gruber et al., 2019), supporting in first approximation the expectation

395   of a steady-state increase in the oceanic storage of C_{ant}. We also note that our ΔC_{ant} column

396   inventory reconstructions for the 1994–2007 period (Fig. S6) confirm those reported by

397   Gruber et al. (2019) for the same period, supporting the consistency of our approaches and

398   estimates despite the modifications of the eMLR(C*) method and our use of an updated

399   database.

400   While the general pattern of the increases in the C_{ant} column inventories are similar in the two

401   decades, there are distinct differences (Fig. 2C). These decadal differences are most

402   pronounced in the Atlantic Ocean, where we find a shift of the highest ΔC_{ant} column

403   inventories from the Northern to the Southern Hemisphere. In the subtropical latitudes (20–

404   50 °N) of the North Atlantic, the mean, area-weighted ΔC_{ant} column inventory in the second

405   decade is 3.7 ± 0.8 mol m^{-2} dec^{-1} lower compared to the first one (1994–2004: 12.1 ± 0.5;

406   2004–2014: 8.4 ± 0.6 mol m^{-2} dec^{-1}; ± 1σ uncertainty). In contrast, the mean ΔC_{ant} column

407   inventory in the subtropical latitudes of the South Atlantic (20–50 °S) is 4.7 ± 2.2 mol m^{-2}

408   dec^{-1} higher in the second decade (1994–2004: 8.5 ± 0.9; 2004–2014: 13.2 ± 1.9 mol m^{-2} dec^{-}

409   ^{1}). In other regions of the ocean, the decadal differences are within or close to the bounds of

410   the uncertainty inferred from the alternative reconstructions. We thus refrain from further

411   analysis. The spatial patterns in the decadal difference of our ΔC_{ant} column inventories are

412   reminiscent of the anomaly structure that Gruber et al. (2019) derived from a comparison of

413   their ΔC_{ant} column inventories to the steady-state projection of the total C_{ant} inventory in 1994

414   from Sabine et al. (2004).
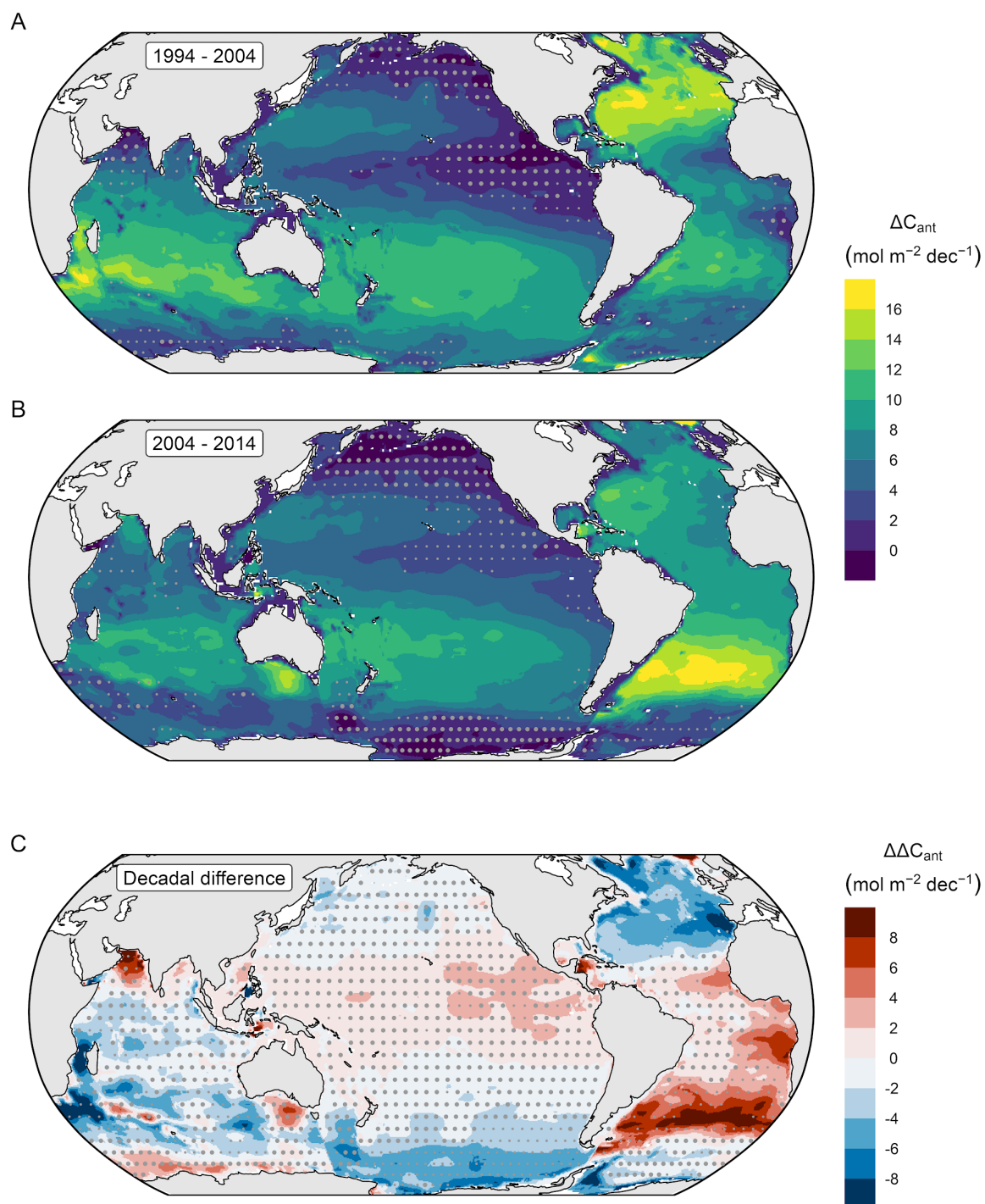
**Fig. 2**: Column inventory maps of the storage change of anthropogenic carbon (ΔC_{ant} in mol m^{-2} dec^{-1}) integrated over the upper 3000m of the ocean for (A) 1994–2004 and (B) 2004–2014. Decadal differences in the storage changes ($\Delta\Delta C_{ant}$) are shown in (C). Plotted here are the results from the standard configuration. Stippling with small or large dots on a 5°x5° grid indicates regions in which the ΔC_{ant} and $\Delta\Delta C_{ant}$ column inventories are lower than the 2σ- or 1σ-uncertainty, respectively.

3.2 Vertical distribution

The high column inventories of ΔC_{ant} in the centres of the subtropical gyres seen in Figure 2A,B are due to a deeper penetration of ΔC_{ant} in these regions. This is illustrated by plotting ΔC_{ant} along a global section (Fig. 3A,B) that connects the zonal mean sections of the Atlantic and Pacific Ocean with a meridional mean section crossing the Indian Ocean sector of the Southern Ocean. Within the subtropical gyres, ΔC_{ant} exceeding 5 µmol kg^{-1} dec^{-1} reaches at least 300 m deeper than in the equatorial regions. This is primarily a consequence of the passive tracer transport of C_{ant} along isopycnal surfaces (depicted in Fig. 3C), which brings C_{ant} more rapidly into the ocean's interior in regions of downward sloping isopycnals (Bopp et al., 2015; DeVries and Primeau, 2011). In the South Pacific, the ΔC_{ant} signal reaches deeper into the water column compared to the North Pacific, which is a persistent pattern for both decades and attributed to the formation of Subantarctic Mode and Antarctic Intermediate Water (SAMW and AAIW). In contrast, in the Atlantic Ocean we identify a shift of the deepest penetration of the ΔC_{ant} level of 5 µmol kg^{-1} dec^{-1} from the Northern to Southern Hemisphere (Fig. 3C).

These changes in the downward extensions of ΔC_{ant} cause the decadal differences identified in the column inventories of ΔC_{ant} in the Atlantic Ocean (Fig. 2C). The decrease of the mean ΔC_{ant} column inventory in the North Atlantic is a consequence of the weaker C_{ant} storage increase in the North Atlantic Deep Water (NADW), evident in the zonal mean section as negative decadal differences (-2 to -5 µmol kg^{-1} dec^{-1}) at neutral densities >27.5 kg m^{-3} (Fig. 3C). In contrast, the decadal increase of the ΔC_{ant} column inventory in the South Atlantic can be attributed to an intensified rate of C_{ant} storage in the Subantarctic Mode Waters (SAMW) and Antarctic Intermediate Waters (AAIW). Here, positive ΔC_{ant} differences in the zonal mean sections are well confined to the neutral density slabs ranging from 26.5 to 27.5 kg m^{-3} (Fig. 3C). The decadal ΔC_{ant} differences in the NADW and the AAIW are larger than the uncertainty of our reconstructions, while in most other water masses, the decadal differences are not significant (stippled regions in Fig. 3C).
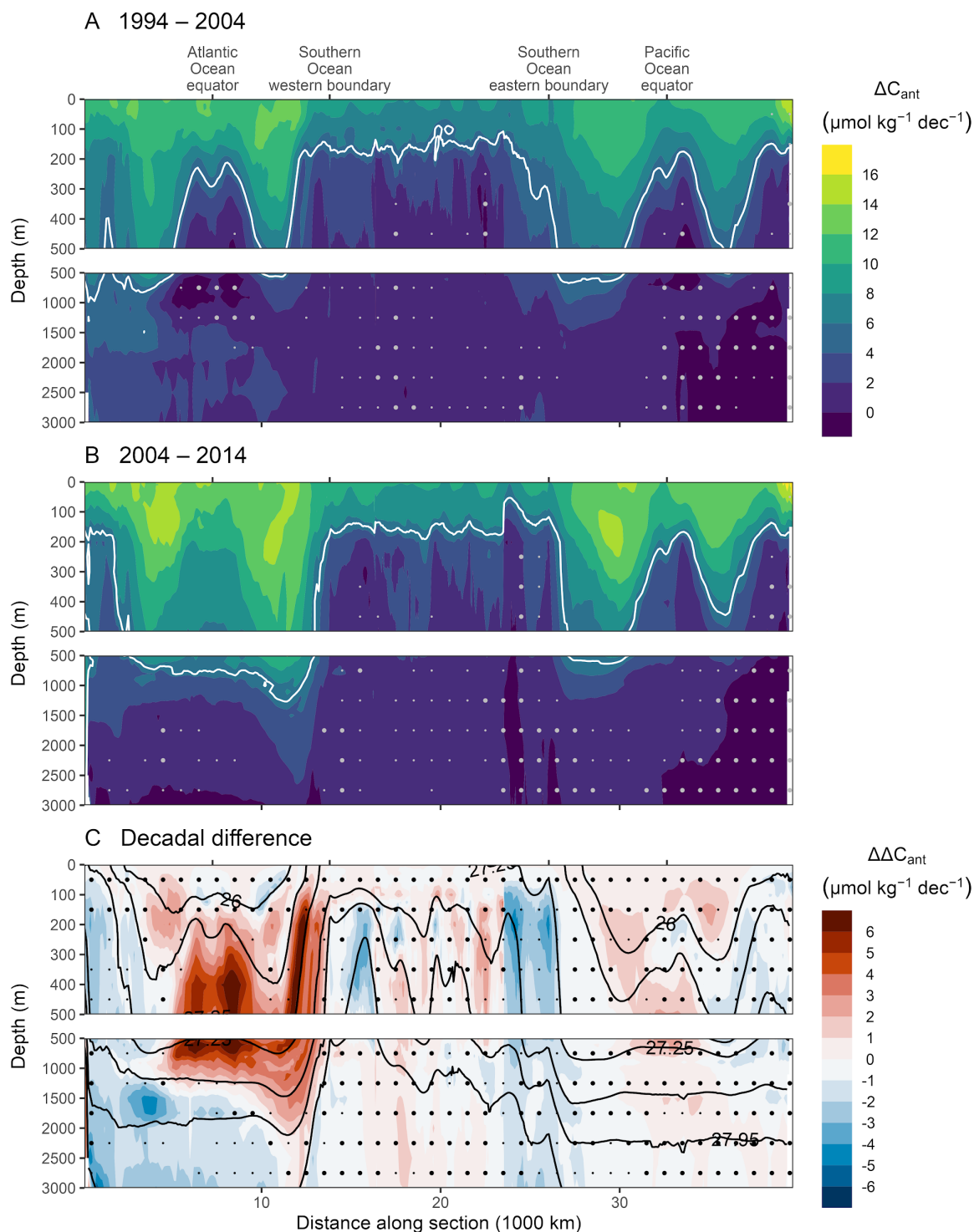
Fig. 3: Global sections of changes in the anthropogenic carbon content from north to south in the Atlantic Ocean, west to east in the Southern Ocean and south to north in the Pacific Ocean. The standard case reconstruction of ΔC_{ant} (in µmol kg^{-1} dec^{-1}) is shown for the decades (A) 1994–2004 and (B) 2004–2014. The white contour lines highlight the ΔC_{ant} level of 5 µmol kg^{-1} dec^{-1}. (C) Decadal differences between the storage changes ($\Delta\Delta C_{ant}$) shown in (A) and (B). Black contour lines in (C) indicate isoneutral density levels. The selected contours represent every second density slab used to cluster the data in the vertical dimension. Stippling with small or large dots indicates regions in which

454   the ΔC_{ant} and $\Delta\Delta C_{ant}$ column inventories are lower than the 2σ- or 1σ-uncertainty, respectively. The

455   North-South sections through the Atlantic and Pacific Ocean show zonal mean values across the

456   entire basins, while the Southern Ocean sector is represented by a meridional mean section ranging

457   from 55 to 65°S.

458   Examining the vertical distribution of the reconstructed ΔC_{ant} in terms of area-weighted mean

459   content profiles (Fig. 4A), we find that globally C_{ant} in the upper 50 m of the ocean increased

460   on average by $10 - 11$ µmol kg^{-1} dec^{-1} in both periods. As the storage change near the surface

461   is determined based on an assumed equilibrium with the atmospheric pCO_2, it shows

462   latitudinal patterns that reflect gradients in the surface ocean buffer capacity (Fig. 3AB).

463   However, regional differences of the surface ΔC_{ant} averaged over hemispheric ocean basins

464   are small (Fig. 4A). Furthermore, the almost identical surface ΔC_{ant} for both decades is due to

465   a compensation of the higher atmospheric pCO_2 growth rate and the reduced surface ocean

466   buffer capacity in the second decade of our analysis. The global mean penetration depth of

467   ΔC_{ant}, which we define as the mean column inventory (Fig. 2) divided by the mean surface

468   content (Fig. 4A), is similar for both decades and extends to 640 ± 45 m and 560 ± 45 m for

469   the 1994–2004 and 2004–2014 periods, respectively. However, this penetration depth varies

470   remarkably across the individual ocean basins. In the North Pacific, the mean penetration

471   depth of ΔC_{ant} does not exceed 300m, while in the Southern Hemisphere, the penetration

472   depth exceeds 600 m in all ocean basins and decades. In the South Atlantic, we find a

473   pronounced deepening of the penetration depth from 630 ± 80 m in the first decade to $870 \pm$

474   100 m in the second decade. In the North Atlantic the penetration depth changes in the

475   opposite direction and decreases from 830 ± 30 m to 670 ± 50 m.

476   The decadal differences in the penetration depth are directly related to patterns in the mean

477   ΔC_{ant} profiles. In the North Atlantic, ΔC_{ant} below 1000m is about 3 µmol kg^{-1} dec^{-1} lower

478   during the second decade (Fig. 4A), while the mean ΔC_{ant} signal in the South Atlantic was

479   significantly higher by about 3 µmol kg^{-1} dec^{-1} between 500 and 1500m during the second

480   decade.
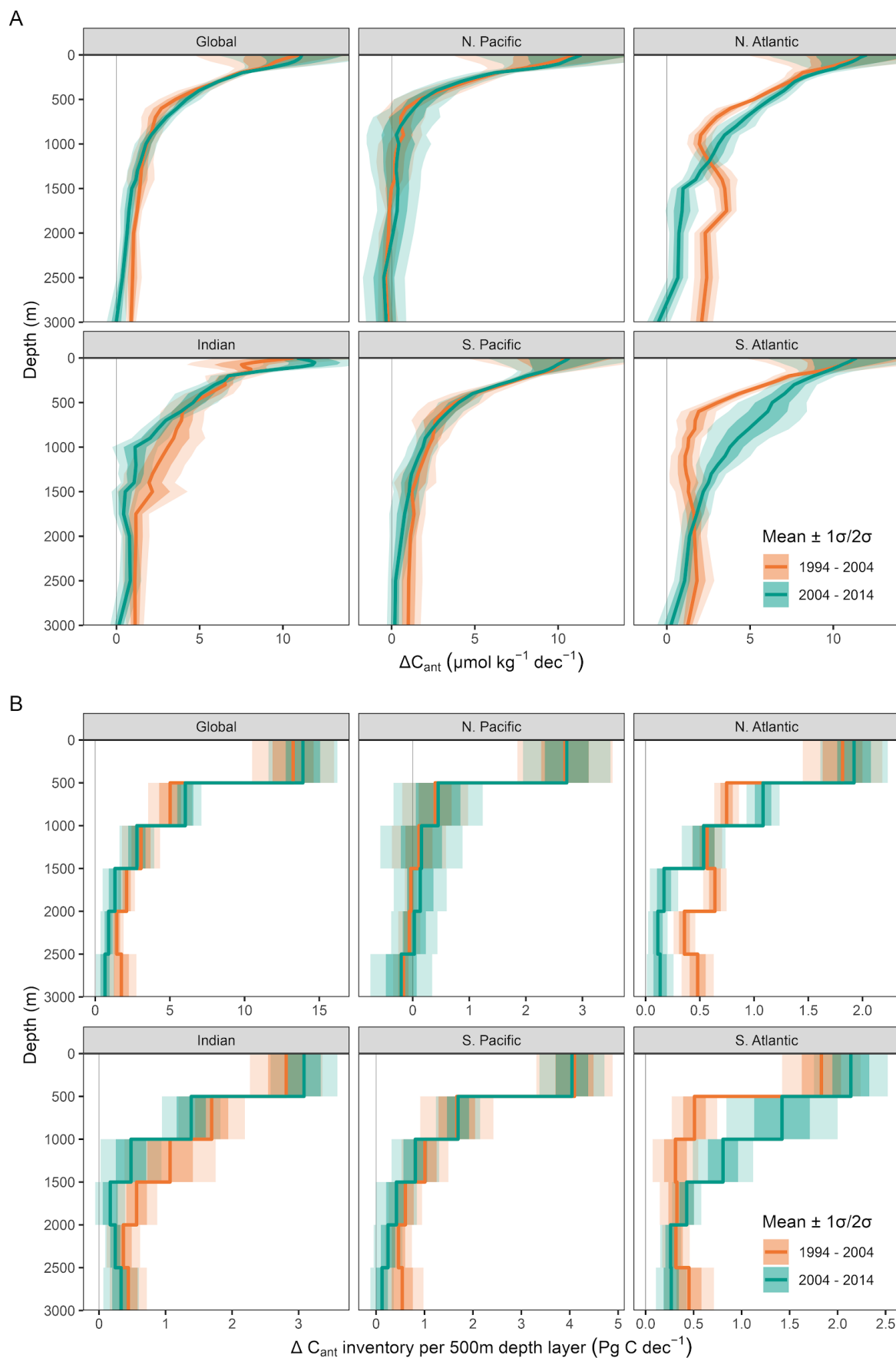
Fig. 4: Mean vertical distribution of the decadal changes in anthropogenic carbon (ΔC_{ant}) for the

482   global ocean and both hemispheres of the main ocean basins. (A) Mean profiles and (B) 500m-depth

483   layer inventories of ΔC_{ant}. Colours distinguish the decades 1994–2004 and 2004–2014. Thick lines

484   represent the standard case reconstruction of ΔC_{ant} and ribbons indicate the 1σ- and 2σ-uncertainty

485   ranges.

3.3 Regional and global inventories

487   Reflecting the rapid decrease of ΔC_{ant} with depth (Fig 4A), almost 50% of the global C_{ant}

488   storage change occurs in the upper 500 m of the water column (Fig. 4B). Over the upper 1000

489   m, this share increases to around 75%, except in the North Pacific, where the entire inventory

490   increase is fully confined to the top 1000 m. In all other ocean regions depicted in Figure 4B,

491   a significant fraction of the C_{ant} storage change occurs below 1000 m (~25% on a global

492   basis) as a result of the more rapid water mass transport and mixing between the surface and

493   ocean interior in these regions. The decadal differences in the ΔC_{ant} inventories for 500 m

494   depth layers reflect the profiles of the amount content and were found to be significant only

495   in the three depth layers below 1500m of the North Atlantic, as well as between 500 and 1500

496   m in the South Atlantic (Fig. 4B).

497   Once integrated over the top 3000 m of entire ocean basins, (Fig. 5 and Table 1), the South

498   Pacific stands out as the region with the highest increase of C_{ant} storage for both decades

499   (1994–2004: 8.6 ± 1.2 Pg C dec^{-1} and 2004–2014: 7.4 ± 1.0 Pg C dec^{-1}), followed by the

500   Indian Ocean (7.2 ± 0.9 and 5.7 ± 0.6 Pg C dec^{-1}). In contrast, the North Pacific accounts for

501   the smallest contribution to the increase in the oceanic storage of C_{ant} in both decades (2.9 ±

502   0.8 and 3.2 ± 1.8 Pg C dec^{-1}). The decadal differences in the increases in C_{ant} storage are not

503   significant at the 2σ-uncertainty level in any of these three regions. This is different for the

504   North Atlantic (Fig. 5, Table 1), which represented the third largest sink region during the

505   1994–2004 decade (4.8 ± 0.2 Pg C dec^{-1}), but experienced a C_{ant} accumulation rate that was

506   significantly reduced by 0.9 ± 0.4 Pg C dec^{-1} during the 2004–2014 period (3.9 ± 0.4 Pg C

507   dec^{-1}). In contrast, the storage rate in the South Atlantic increased by 1.5 ± 0.8 Pg C dec^{-1}

508   from the first (3.9 ± 0.5 PgC dec^{-1}) to the second decade (5.4 ± 0.6 Pg C dec^{-1}) of our analysis.

509   As a consequence, the South Atlantic represents the third largest contributor to the global

510   accumulation of C_{ant} from 2004 to 2014. The ranking of the ocean basins in terms of their

511   contribution to the global ocean C_{ant} sink reflects primarily the differences in surface area of

512   the basins.

513   In terms of the storage efficiency normalised to the surface area, i.e. $\beta = \Delta C_{ant} / \Delta pCO_{2,atm}$

514   (mol m^{-2} µatm^{-1}), the ranking of the regions changes markedly (Table 1 and Fig. S5). The

515   North Atlantic reveals the highest regional storage efficiency (25–40% larger than the global

516   mean), and the North Pacific the lowest one (about 45–55% lower than the global mean).

517   This largely reflects the differences in intermediate, mode, and deep water formations

518   between the different basins, and will be further discussed in section 4.1.
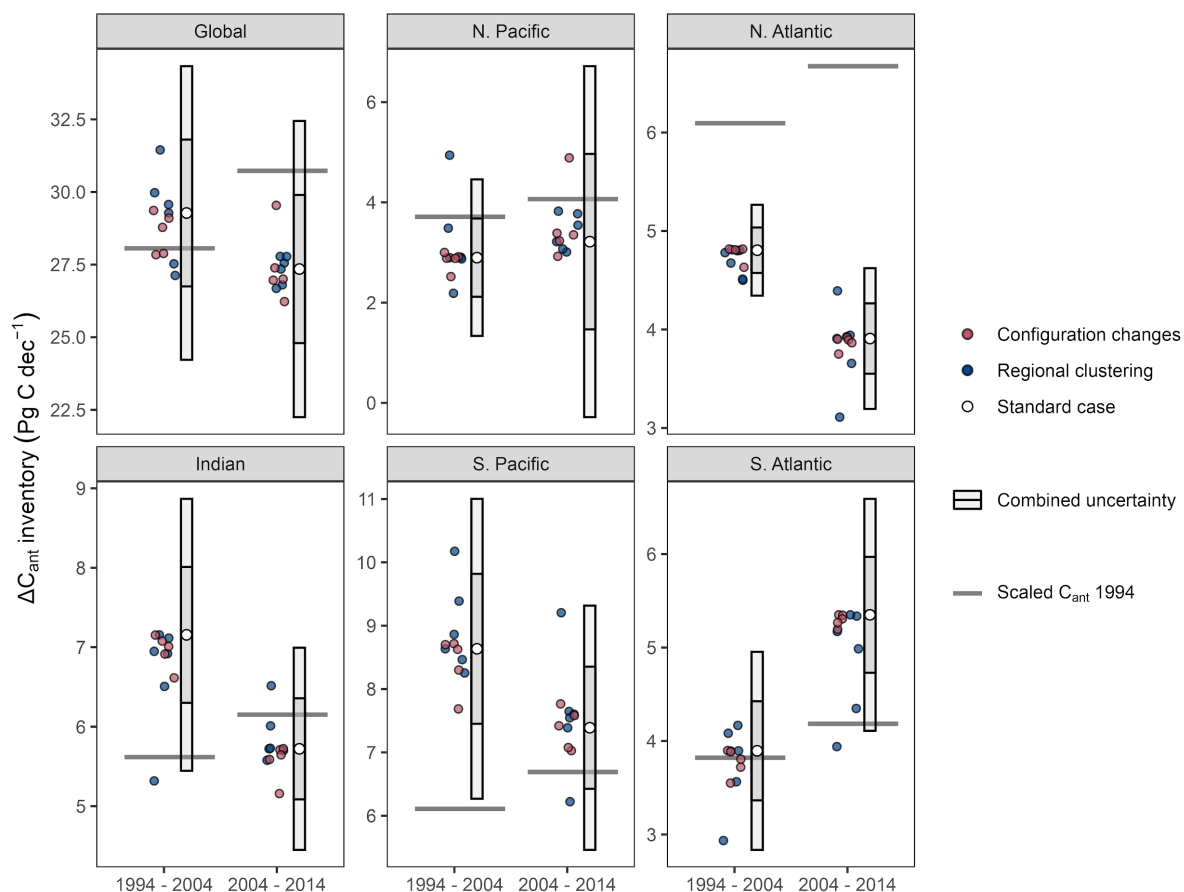
519   **Fig. 5**: Inventories of the change in the anthropogenic carbon storage (ΔC_{ant} in Pg C dec^{-1}) for each

520   hemisphere of the main ocean basins and the global ocean, and the decades 1994–2004 and 2004–

521   2014. White symbols represent the standard case of our ΔC_{ant} reconstructions and error bars the 1σ-

522   and 2σ-uncertainty range. Horizontal lines indicate projected inventories based on the total C_{ant}

523   storage in 1994 (Sabine et al., 2004) and assuming proportional growth with atmospheric CO_2.

524   Coloured points represent ΔC_{ant} reconstructions considered in the uncertainty assessment (red:

525   configuration changes of the eMLR(C*) method; blue: regional clustering) and are arbitrarily spaced

526   in the horizontal direction for visibility.

527   When integrating ΔC_{ant} globally and scaling it for unmapped regions and deep water storage,

528   we determine an ocean sink for anthropogenic CO_2 that amounts to 29.3 ± 2.5 and 27.3 ± 2.5

529   Pg C dec^{-1} for the 1994–2004 and the 2004–2014 decade, respectively (Fig. 5, Table 1).

530 These inventory changes of C_{ant} are indistinguishable for both decades with a difference of -

531 1.9 ± 3.6 Pg C dec^{-1}, indicating that the global ocean continued to act as a strong sink for

532 anthropogenic CO_2 in the recent past. The efficiency β of the global C_{ant} sink decreased

533 markedly and significantly, however, from 0.37 ± 0.03 mol m^{-2} µatm^{-1} for the decade 1994–

534 2004 to 0.31 ± 0.03 mol m^{-2} µatm^{-1} during the second decade 2004–2014 (Table 1). For the

535 20-year period from 1994–2014, the directly estimated global ΔC_{ant} inventory is identical to

536 the sum of the estimates from the individual decades (56.7 ± 3.5 Pg C dec^{-1}).

537 **Table 1**: Inventories of the change in anthropogenic carbon storage (ΔC_{ant} in Pg C dec^{-1}) and the

538 corresponding sink efficiency (β = ΔC_{ant} / $\Delta pCO_{2,atm}$ in mol m^{-2} µatm^{-1}) for the first (1994–2004) and

539 second (2004–2014) decade of our analysis. Inventories are integrated separately across both

540 hemispheres of the main ocean basins and the global ocean. All values refer to the standard cases of

541 our ΔC_{ant} reconstruction and the 1σ-uncertainty ranges. Decadal inventory differences are tagged with

542 ** or * when they exceed the combined 2σ- or 1σ-uncertainty of both decades, respectively.

Region	Estimate	1994–2004	2004–2014	Decadal difference
Global	ΔC_{ant}	29 ± 2.5	27 ± 2.5	-1.9 ± 3.6
	β	0.37 ± 0.03	0.31 ± 0.03	-0.05 ± 0.04 *
Indian	ΔC_{ant}	7.2 ± 0.9	5.7 ± 0.6	-1.4 ± 1.1 *
	β	0.44 ± 0.05	0.32 ± 0.04	-0.12 ± 0.06 *
N. Pacific	ΔC_{ant}	2.9 ± 0.8	3.2 ± 1.8	0.3 ± 1.9
	β	0.17 ± 0.05	0.17 ± 0.09	0.002 ± 0.1
S. Pacific	ΔC_{ant}	8.6 ± 1.2	7.4 ± 1.0	-1.2 ± 1.5
	β	0.40 ± 0.06	0.31 ± 0.04	-0.09 ± 0.07 *
N. Atlantic	ΔC_{ant}	4.8 ± 0.2	3.9 ± 0.4	-0.9 ± 0.4 **
	β	0.53 ± 0.03	0.39 ± 0.04	-0.14 ± 0.04 **
S. Atlantic	ΔC_{ant}	3.9 ± 0.5	5.4 ± 0.6	1.5 ± 0.8 *
	β	0.39 ± 0.05	0.49 ± 0.06	0.1 ± 0.08 *

543 **3.4 Uncertainty assessment**

544 Nearly all identified main configuration choices of the eMRL(C*) method matter for the

545 reconstruction of the decadal increases in C_{ant} and contribute to the uncertainties of the global

546 inventory changes of about ±10% (Table 1, Figs. 6 and S9). The smallest uncertainty

547 contributions stem from alternative definitions of C* and from uncertainties associated with

548   the predictor climatologies used for mapping (Fig. 6). All other configuration choices matter
549   more, although differently for the two decades, largely reflecting differences in the data
550   distribution and data consistency.
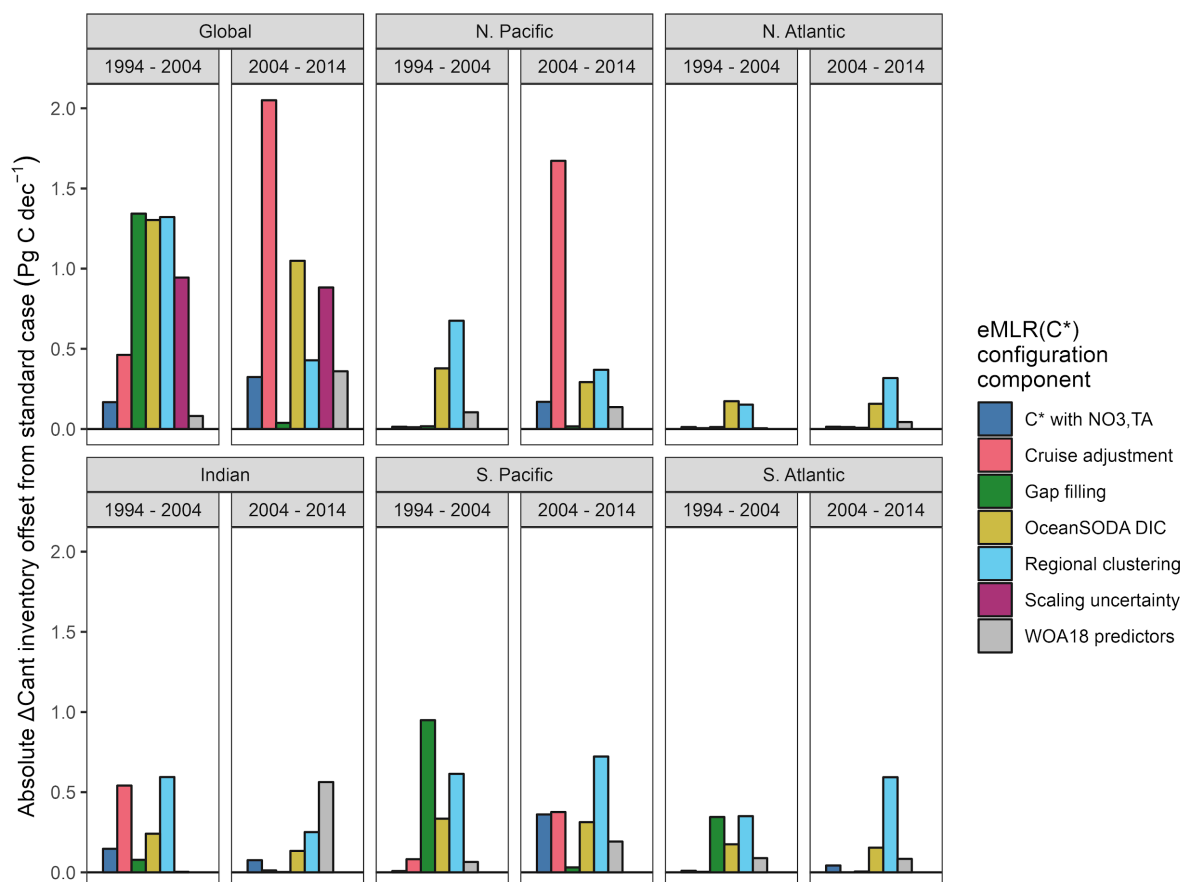
551   **Fig. 6**: Inventory uncertainty contributions at the 1σ-uncertainty level determined as offsets between
552   our standard case reconstruction and six configuration choices of the eMLR(C*) method (colours) for
553   each ocean region and both decades (panels). All offsets are shown as absolute values. The
554   uncertainty contribution that accounts for our upscaling for unmapped water masses is shown for the
555   global inventory.

556   The single largest contribution to the global inventory uncertainty comes from the way we
557   applied the adjustments to the DIC, TA and PO_4^{3-} measurements in order to ensure the highest
558   level of data consistency. If the adjustments were determined and applied separately for each
559   cruise instead of in a bulk manner as done in the standard configuration, the global ΔC_{ant}
560   inventories change by ~-0.5 Pg C dec^{-1} during the 2004-2014 period, and by ~+1.5 Pg C dec^{-1}
561   for the 2004-2014 period. Nearly all of the changes during the earlier decade originate at the
562   Indian Ocean, while those for the second period originate at the North Pacific (Figs. 6 and

563   S9), as expected given that these were the regions where we applied these adjustments.

564   The second most important uncertainty contribution comes from the regional clustering of the
565   observations with uncertainty contributions to the regional inventories ranging from 0.2 to 0.8
566   Pg C dec^{-1} (Figs. 6 and S9). However, for the global ΔC_{ant} inventories, the uncertainties
567   arising from the regional clustering partially cancel out, such that the global uncertainty
568   contribution is lower than the sum of the uncertainties in the individual basins (<1.5 Pg C
569   dec^{-1} for both decades, Fig. 6).

570   Among the other choices, the approach for the surface ΔC_{ant} reconstruction contributes about
571   1 Pg C dec^{-1} to the uncertainty of the global ΔC_{ant} inventory, determined by comparing our
572   estimate based on the assumption of surface ocean equilibrium of C_{ant} with a reconstruction
573   based on observation-based surface changes of DIC (Gregor and Gruber, 2021). Choices
574   associated with the gap filling also contribute about 1 Pg C dec^{-1} to the global uncertainty, but
575   this error source is limited largely to the first decade and the South Pacific (Fig. S9), where
576   we had to include a substantial number of cruises that took place in the 1990s and provided
577   only calculated TA data (Fig. 1). Finally, our scaling of the ΔC_{ant} inventories for unmapped
578   regions and the deep ocean introduces an additional uncertainty contribution of about 1 Pg C
579   dec^{-1}, however, confined to the global ΔC_{ant} inventories and of very similar magnitude for
580   both decades.

581   In addition to investigating the contribution of the configuration choices to the uncertainty of
582   our standard configuration, we also determined the sensitivity of our results to a set of
583   additional decisions we had to take for our reconstructions (see section S4.2). We did not add
584   these results to our formal uncertainty estimate since we consider our choices as well
585   justified, and the alternatives as clearly inferior choices. Analogous to our finding above for
586   the contribution to the assessed uncertainty, we find that the biggest sensitivity of the results
587   is associated with the data adjustments. Reconstructions of ΔC_{ant} based on the unadjusted data
588   reveal biases (Fig. S11 and S12) that are more than a factor of two larger than our estimated
589   adjustment uncertainty. Furthermore, we tested the sensitivity of our results to data coverage
590   by reconstructing ΔC_{ant} with observations only from cruise sections that were reoccupied
591   during both sampling periods. This reoccupation filter has generally a low impact on the
592   reconstructed column inventories and basin inventories (Fig. S11 and S12), suggesting an
593   overall sufficient data coverage. An exception to this are the ΔC_{ant} reconstructions in the

594   Indian Ocean, which are more sensitive to the reoccupation filter (Fig. S11) due to the lack of

595   data from the Arabian Sea during the central sampling period, i.e., the 2000s (Fig. 1B).

596   Our observation-based uncertainty and sensitivity findings are corroborated by our tests with

597   synthetic data generated from an ocean hindcast model (supplement S5), following the

598   approach developed by Clement and Gruber (2018). Comparing the biases of our

599   reconstructed model inventories to the estimated uncertainty based on the configuration

600   choices, we find that the bias of 7 (11) out of 12 reconstructed ΔC_{ant} inventories is within the

601   1σ- (2σ-) uncertainty range (Fig. S18), which meets the expectation of a 68% (95%)

602   confidence interval. Our uncertainty ranges and confidence intervals are thus considered

603   suitable criteria to evaluate the significance of our ΔC_{ant} reconstructions. Furthermore, the

604   eMLR(C*) method proves capable of reconstructing the global ΔC_{ant} patterns (Fig. S13). The

605   reconstruction biases of the ΔC_{ant} column inventories are below 2 mol m^{-2} dec^{-1} for 87% of the

606   total ocean surface area, within 2 – 4 mol m^{-2} dec^{-1} for 13%, and only exceed the latter

607   threshold for <0.5% of the surface area. In contrast, the true ΔC_{ant} column inventories in our

608   model are larger than these thresholds of 2 and 4 mol m^{-2} dec^{-1} over more than 90 and 55% of

609   the surface area of the ocean, respectively (Fig. S13A). In agreement with this assessment

610   based on synthetic data, the observation-based ΔC_{ant} column inventories exceed the 1σ- and

611   2σ-uncertainty level over more than 90 and 75% of the total ocean surface area (Fig. 2A).

612   ΔC_{ant} column inventories that are lower than the local uncertainty are confined to regions with

613   low ΔC_{ant} column inventories, primarily in the North Pacific (Fig. 2A). We conclude that the

614   global distribution patterns of ΔC_{ant} are robustly reconstructed, which is in line with previous

615   assessments of the method (Clement and Gruber, 2018) despite the shorter sampling periods

616   applied in this study.

617   While the tests with synthetic data demonstrate the ability of the eMLR(C*) method to

618   reconstruct spatial patterns in ΔC_{ant}, the low decadal variability of the current generation of

619   ocean hindcast models (Hauck et al., 2020) impedes the assessment of the method's ability to

620   detect decadal differences in the C_{ant} storage rates ($\Delta \Delta C_{ant}$). As a consequence of the model's

621   low decadal variability, the spatial patterns in the column inventory biases show a strong

622   correlation with the reconstructed $\Delta \Delta C_{ant}$ (Fig. S14 and S15). However, the observation-based

623    $\Delta \Delta C_{ant}$ column inventories in the Atlantic Ocean (Fig. 2B) are higher than the $\Delta \Delta C_{ant}$ biases

624   in the tests with synthetic data by about a factor of two (Fig. S15), suggesting that the

625   observation-based $\Delta \Delta C_{ant}$ patterns carry, at least in part, a true signal.

626   **3.5 Comparison with regional estimates**

627   As a final component to assess the robustness of our estimates, we compare our ΔC_{ant}

628   reconstructions to previous regional estimates that — same as our study — resolve changes

629   for at least two periods and apply an MLR approach to ocean interior observations (see

630   supplement S6 for details). Regional studies that fulfil these criteria are available for the

631   North and South Atlantic (Woosley et al., 2016; Wanninkhof et al., 2010; Gao et al., 2022),

632   as well as the North and South Pacific (Carter et al., 2019). We conclude from this

633   comparison that the magnitude, patterns and trends in our ΔC_{ant} reconstructions agree with

634   those determined in regional studies, and that differences can — where they exist — be

635   attributed to differences in the chosen integration depth, differences in the definition of the

636   target variable C*, and sometimes also to the uncertainty associated with the computation of

637   a whole basin inventory from a single reoccupied transect (Woosley et al., 2016; Gao et al.,

638   2022).

639   The most pronounced difference to a regional estimate exists in the South Pacific, where

640   Carter et al. (2019) determined a change of the C_{ant} inventory of 5.4 ± 0.6 Pg C dec^{-1} from

641   1995 to 2005, whereas we determine a substantially higher inventory change of 8.6 ± 1.2 Pg

642   C dec^{-1} for almost the same period (1994 – 2004). A main difference between these studies is

643   the calculation of C* without (Carter et al., 2019) or with (this study) a TA contribution. Our

644   sensitivity reconstruction of ΔC_{ant} in the South Pacific without considering the contribution of

645   TA for the calculation of C* indeed reveals an inventory change that is about 3 Pg C dec^{-1}

646   lower than our standard case reconstruction. Carter et al. (2019) relied on a synthetic data

647   sensitivity test that included synthetic measurement uncertainties to conclude that the eMLR

648   results are more robust for their implementation when the TA adjustment is omitted from the

649   C* calculation. However, methodological differences between the methods used in that and

650   our study limit the applicability of their sensitivity tests for our approach. We further contend

651   that the additional attention paid to TA quality control results in better TA consistency

652   between cruises than is assumed by Carter et al. (2019) and that the possibility of DIC

653   changes driven by the calcium carbonate cycle (that are neither well represented in the

654   synthetic data nor sufficiently correlated with nutrient and oxygen changes that they would be

655   removed by following the eMLR approach) should not be neglected.

656   The second largest difference from a regional ΔC_{ant} inventory exists in the North Atlantic

657   Ocean, where Wanninkhof et al. (2010) determined a C_{ant} storage rate of only 1.9 ± 0.4 Pg C

658   dec^{-1} for the 1989–2003 period based on a single reoccupied cruise section. Their estimate is

659   drastically lower than ours for the 1994–2004 decade (4.8 ± 0.2 Pg C dec^{-1}). Our tests of the

660   eMLR(C*) method reveal that the uncertainty of our estimates can only explain a minor part

661   of this offset. We conclude that the offset is primarily due to differences in the integration

662   depth, structural uncertainties in the regional estimate (Wanninkhof et al., 2010) and

663   extrapolation errors from a single reoccupied cruise section to a whole basin inventory. In

664   fact, Woosley et al. (2016) found that the whole basin inventories of the North Atlantic differ

665   by ~30% when comparing estimates obtained from a single section to those obtained from

666   three sections.

667   In general, the individual differences between our regional ΔC_{ant} inventories and those

668   obtained in the previous regional studies are within the uncertainty range of our global

669   inventory. Therefore, we do not assume that offsets at the regional scale challenge the

670   robustness and interpretation of our global inventories.

671   **4 Discussion**

672   **4.1 Decadal trends or *the ocean at a time of change***

673   In this study we found that the rates of the increases of the global oceanic storage of

674   anthropogenic carbon for the two consecutive decades since 1994 are indistinguishable, i.e.,

675   29.3 ± 2.5 Pg C dec^{-1} and 27.3 ± 2.5 Pg C dec^{-1} for the 1994–2004 and the 2004–2014 decade,

676   respectively (Fig. 5, Table 1). Putting this continued accumulation of anthropogenic carbon

677   into the context of the total oceanic C_{ant} storage for 1994 (118 ± 19 Pg C), we identify an

678   almost perfect linear correlation with the increase in atmospheric pCO_2 (Fig. 7, see also

679   Gruber et al., in press). For a more detailed and quantitative discussion of the recent decadal

680   trends in the ocean carbon sink, it is thus informative to relate the storage changes in C_{ant} to

681   the increase in atmospheric pCO_2, i.e. in terms of the efficiency β (see section 3.3).

682   At the global scale, we find that the ocean's efficiency to accumulate anthropogenic carbon

683   shows first signs of a weakening, i.e., β decreased significantly by 15% from 0.37 ± 0.03 mol

684   m^{-2} µatm^{-1} during the 1994–2004 decade to 0.31 ± 0.03 mol m^{-2} µatm^{-1} during the 2004 to

685   2014 decade (Table 1, Figs. 7 and 8). In contrast, the reduction of the accumulation of C_{ant}

686   from the first to the second decade by 1.9 ± 3.6 Pg C dec^{-1} represents only a 7% decrease and

687   is not significant. The fact that the decadal decline in β is more robust than that of the ΔC_{ant}

688   inventory itself is due to the ~10% higher growth rate in atmospheric pCO$_2$ from 2004 to

689   2014 ($\Delta pCO_{2,atm}$ = 20.4 µatm dec^{-1}) compared to that during the previous decade from 1994 to

690   2004 (18.6 µatm dec^{-1}).
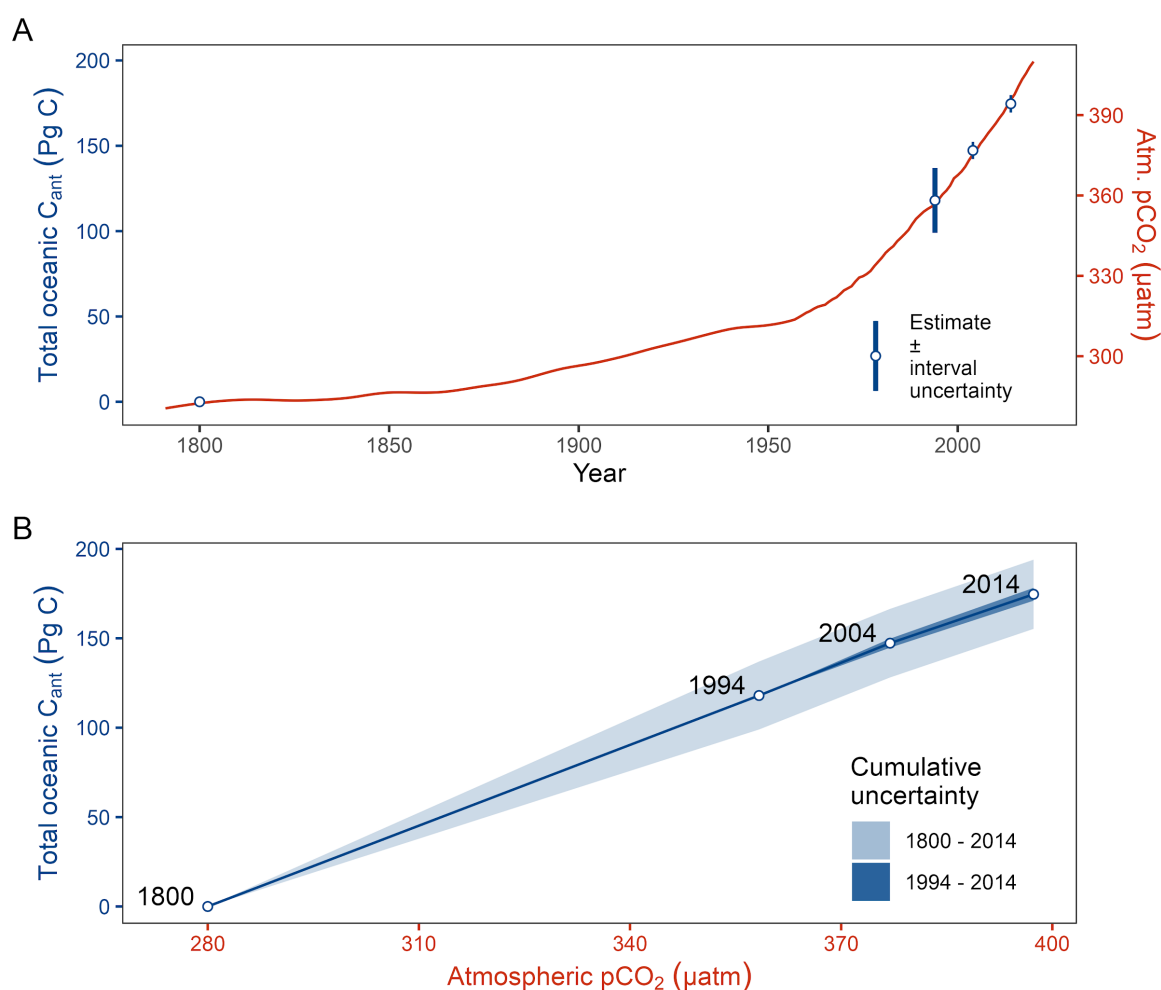
691   **Fig. 7**: Total C_{ant} accumulation in the ocean interior from 1800–2014, shown in blue as a function of

692   (A) time and (B) atmospheric pCO$_2$. Total C_{ant} was estimated by adding our global ΔC_{ant} inventories

693   (Table 1) to the total C_{ant} inventory in 1994 (118 ± 19 Pg C) according to Sabine et al. (2004). The red

694   line in (A) shows the time history of atmospheric pCO$_2$. The cumulative uncertainty in (B) for the

695   1994–2014 period (dark blue ribbon) assumes zero uncertainty in 1994.

696   As the ocean acidifies in response to taking up CO_2, a decrease of the ocean sink efficiency is

697   expected due to the decrease of the ocean buffer capacity (Jiang et al., 2019). Over the past

698   40 years, seawater that followed the same pCO_2 increase as the atmosphere would have

699   experienced a ~6% reduction of the DIC increase per change in pCO_2 roughly every ten years

700   according to fundamental marine CO_2-system considerations. This 6% decadal weakening of

701   the ability of the surface ocean carbonate chemistry to buffer the increase in pCO_2 would

702   explain about half of the observed decrease in the sink efficiency. The other half is most

703   likely attributable to changes in the ocean's circulation and upper ocean stratification (Sallée

704   et al., 2021) that appears to have led to a less efficient downward transport of C_{ant}, which we

705   discuss further in the following.

706   Roughly half of the decrease of the global ocean carbon sink stems from the reduced decadal

707   storage changes in the North Atlantic (-0.9 ± 0.4 Pg C dec^{-1}). Here, we find a significant

708   weakening of the sink efficiency β (-0.14 ± 0.04 mol m^{-2} μatm^{-1}) when comparing the first

709   (1994–2004) to the second decade (2004–2014) of our analysis (Table 1, Figs. S4,S5).

710   Furthermore, our β estimates for both decades are well below that obtained for the 1800–

711   1994 period (Sabine et al., 2004), indicating a progressive weakening of the sink efficiency in

712   the North Atlantic. The most plausible explanation for this progressive weakening is a

713   tendency of the Atlantic Meridional Overturning Circulation (AMOC) to weaken since the

714   1980s (Latif et al., 2022; Jackson et al., 2022, 2019). Attributing the decadal ΔC_{ant} differences

715   to changes in AMOC strength is supported by the localization of the negative $\Delta\Delta C_{ant}$ signal in

716   the North Atlantic Deep Water (Fig. 3C). This view is also in line with two previous sets of

717   regional studies: (i) (Pérez et al., 2010, 2013) found that the C_{ant} storage rates in the North

718   Atlantic subpolar gyre during the phase of a low North Atlantic Oscillation (NAO) from

719   1997–2006 were ∼48% lower than those during the first half of the 1990s, when a high NAO

720   phase was dominant, although the mechanistic processes linking the NAO, subpolar

721   convection strength, gyre circulation and the AMOC are not yet fully understood. (ii)

722   Raimondi et al. (2021) reconstructed C_{ant} column inventories in the Central Labrador Sea

723   based on CFC-12 observations and identified a period of near zero C_{ant} increases between

724   2003 and 2012.

725   However, an important caveat regarding our finding of a progressively weakening North

726   Atlantic C_{ant} sink is the fact that the available ocean interior observations in the North

727   Atlantic stem mostly from the first half of our last sampling period, the 2010s. However, past

728   2013 the NAO switched to a strong positive phase (Holliday et al., 2020) and in line with this

729   the C_{ant} column inventories in the Central Labrador Sea rapidly increased (Raimondi et al.,

730   2021). Likewise, a deep convection event in the Irminger Sea in winter 2014/15 injected

731   anthropogenic carbon into the ocean interior and almost tripled the storage rates compared to

732   those determined from previous hydrographic sections (Fröb et al., 2016). It is thus possible

733   that our reconstructions do not capture a very recent reinvigoration of the North Atlantic C_{ant}

734   sink, due to the temporal distribution of observations.

735   The decadal difference of the South Atlantic C_{ant} sink is significant on the 1σ-uncertainty

736   level (+1.5 ± 0.8 Pg C dec^{-1}) and slightly exceeds the increase expected from the growth in

737   atmospheric pCO$_2$ alone, expressed in an increase of the sink efficiency (+0.1 ± 0.08 mol m^{-2}

738   µatm^{-1}). In contrast to the North Atlantic, the decadal change in the South Atlantic is not of

739   progressive nature when putting it into context of the total C_{ant} storage until 1994 (Fig. 5), i.e.

740   only the second decade reveals a tendency towards an elevated storage efficiency. Due to the

741   strong spatial coherence between the positive $\Delta\Delta C_{ant}$ signal and the Subantarctic Mode and

742   Antarctic Intermediate Waters (Fig. 3C), we attribute the decadal differences found in the

743   South Atlantic to increased ventilation rates of these water masses (Patara et al., 2021;

744   DeVries et al., 2017; Shi et al., 2021).

745   Although the decadal inventory changes in the Indian Ocean and South Pacific are much less

746   robust than those in the Atlantic, they represent in sum a contribution of about 2.6 ± 1.9 Pg C

747   dec^{-1} to the decline of the global inventory. As the negative $\Delta\Delta C_{ant}$ signals in these regions are

748   associated primarily with the location of Antarctic Bottom Water and Lower Circumpolar

749   Deep Waters (Fig. S7), the decadal differences in the C_{ant} storage changes are likely a

750   consequence of circulation changes as well, albeit determined with lower uncertainty than in

751   other regions.

752   An additional, and globally perhaps more uniform, contribution to the decrease may stem

753   from the observed increase in upper ocean stratification (Sallée et al., 2021). Sallée et al.

754   found that the density contrast across the base of the mixed layer had increased by about 9%

755   per decade between 1970 and 2018. Although their estimate pertains only to the summer,

756   such an increase in stratification is bound to decrease the transport of C_{ant} from the surface to

757   depth, i.e., the most important bottleneck for the uptake of C_{ant} from the atmosphere.

758   We conclude that in addition to the decrease of the ocean buffer capacity, ocean circulation

759   changes and the increase in stratification are the primary reason for the decrease in the

760   efficiency of the oceanic sink for anthropogenic carbon.

761   **4.2 Comparison with observation-based surface flux estimates: Implications for changes**

762   **in natural CO_2**

763   In the following, we compare our estimates of the ocean carbon sink to an ensemble of

764   independent observation-based constraints, namely the surface CO_2 flux products assembled

765   by the Global Carbon Budget (Friedlingstein et al., 2022). During the 1994–2004 decade, the

766   ocean interior accumulation of anthropogenic carbon (29.3 ± 2.5 Pg C dec^{-1}) exceeds the

767   time-integrated net air-sea flux of CO_2 of 21.4 ± 2.8 Pg C dec^{-1} (Fig. 8 and Table 2). For this

768   comparison, we adjusted the observation-based air-sea fluxes for a preindustrial steady-state

769   outgassing of riverine CO_2 of 6.1 Pg C dec^{-1} (Jacobson et al., 2007; Resplandy et al., 2018)

770   without considering the uncertainty contribution from this adjustment. We further excluded

771   the estimates provided by Watson et al. (2020) when calculating the ensemble mean and

772   standard deviation of the flux products. Analogous to Gruber et al. (2019), the difference

773   between the ocean interior estimates and the surface fluxes of 7.9 ± 3.8 Pg C dec^{-1} can

774   plausibly be interpreted as a loss of natural carbon from the ocean to the atmosphere (Table

775   2). Such natural carbon fluxes are captured by the surface flux products, but are not included

776   in the eMLR(C*) based estimates of the accumulation of C_{ant} in the ocean's interior (Clement

777   and Gruber, 2018). The 1σ-uncertainty of this residual term is almost half as large as the

778   signal itself, suggesting that the determined flux is significant, but its magnitude not well

779   constrained. However, postulating a loss of natural carbon for the first decade of our analysis

780   is qualitatively in line with previous studies, which concluded that the stagnation of the ocean

781   carbon sink during the 1990s is due to an anomalously strong outgassing of natural carbon

782   primarily in the Southern Ocean (Landschützer et al., 2015; Lovenduski et al., 2008; Le

783   Quéré et al., 2007).

784   For the 2004–2014 decade, there is no significant difference between the cumulative surface

785   CO_2 fluxes (26.5 ± 1.3 Pg C dec^{-1}) and our ocean interior ΔC_{ant} inventory (27.3 ± 2.5 Pg C

786   dec^{-1}), suggesting only a minor global net flux of natural CO_2 across the air-sea interface (0.9

787   ± 2.9 Pg C dec^{-1}). The fact that during the second decade the gain of anthropogenic and the

788   loss of natural carbon weakened simultaneously can plausibly be explained by a weakened

789 ventilation of the ocean interior, induced by changes in circulation and/or stratification

790 (Sallée et al., 2021), which results in lower upward transport rates of natural carbon to the

791 surface and, vice versa, reduced downward transport of C_{ant} into the ocean interior. This

792 coupling was already hypothesised in previous studies that identified a synchronised

793 reduction of both carbon flux components during periods of a weak upper-ocean overturning

794 circulation (DeVries et al., 2017; Lovenduski et al., 2008). Specifically, DeVries et al. (2017)

795 suggested a more vigorous global overturning in the 1990s that drove an increased

796 outgassing of natural CO_2 and uptake of anthropogenic CO_2, whereas a weaker overturning in

797 the 2000s was found to have the opposite effect. Although the periods of our and their study

798 do not fully overlap, the tendencies toward a weaker anthropogenic carbon uptake agree.

799 The synchronisation of the uptake of anthropogenic and the outgassing of natural carbon was

800 also observed at a regional scale in the Irminger Sea, where Fröb et al. (2018) detected a

801 sharp increase of the C_{ant} inventory from 2012 to 2015, accompanied by a decline in the

802 natural carbon inventory. This was attributed to a deep convection event during 2015 (Fröb et

803 al., 2016), and underlines that variability at regional scale can superimpose upon the

804 postulated global trend towards a declining anthropogenic carbon uptake.
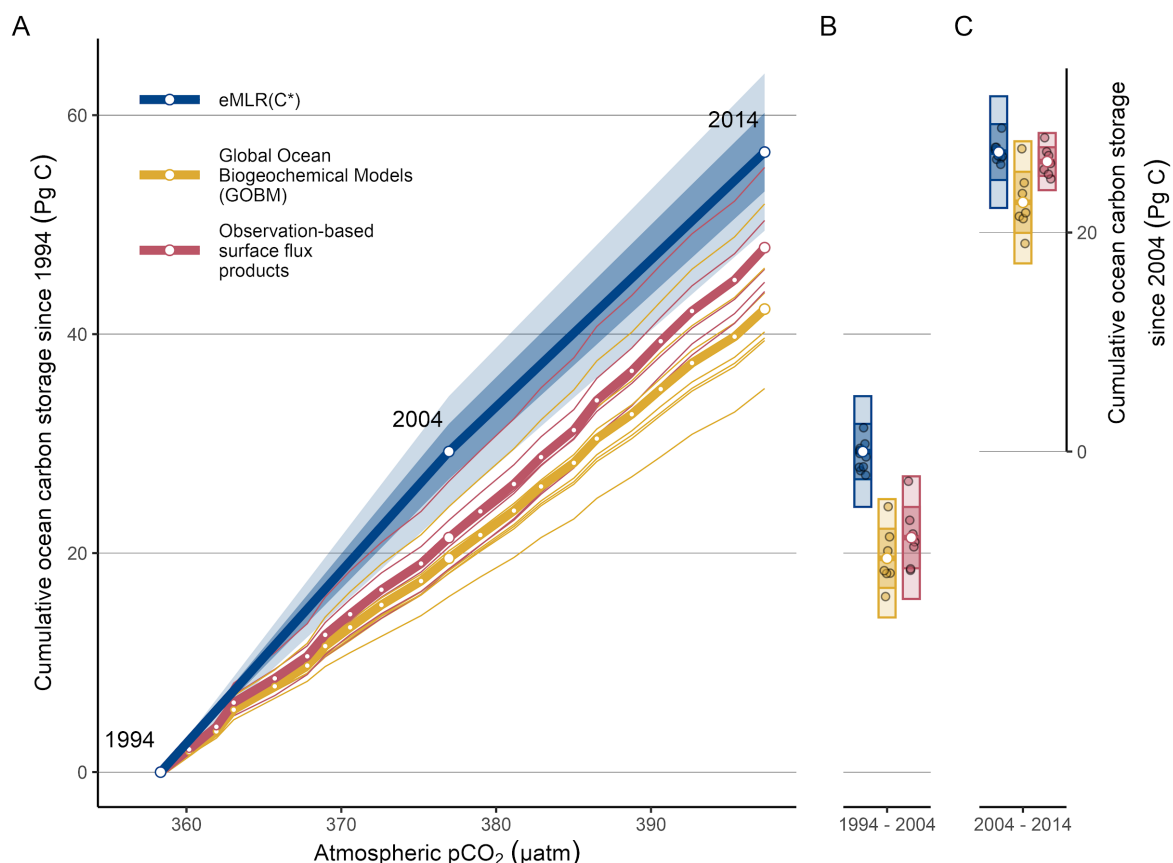
Fig. 8: Ocean carbon storage from 1994 to 2014 according to the eMLR(C*) estimates from this study
(blue), in comparison to the cumulative fluxes from surface pCO_2 observation-based air-sea CO_2 flux
products (red) and Global Ocean Biogeochemical Models (yellow) from the Global Carbon Budget.
The ocean carbon storage is displayed in (A) as a function of atmospheric pCO_2 and in (B and C) as
separate temporal integrals across the two decades of our study. All cumulative estimates for the
2004–2014 period in (C) use the eMLR(C*) estimate for 2004 as the zero point. White points
represent the ensemble mean for the GCB estimates and the standard case for the eMLR(C*)
estimates. Bars in (B and C) indicate 1σ- and 2σ-uncertainty ranges. Note: The eMLR(C*) estimates
represent storage changes of anthropogenic carbon only, while the GCB estimates include fluxes of
natural and anthropogenic CO_2 (see detailed discussion in the main text).

4.3 Implications for the Global Carbon Budget and climate change

During the first decade of our study (1994–2004), the flux estimates of the GOBMs (19.5 ±
2.7 Pg C dec^{-1}) and the observation-based flux products (21.4 ± 2.8 Pg C dec^{-1}) are
significantly lower than the eMLR(C*)-based estimate (29.3 ± 2.5 Pg C dec^{-1}). In the
previous section, we proposed climate-driven outgassing of natural CO_2 from the ocean as a
plausible explanation for the discrepancy to the surface flux products. The same argument

821 would apply to the GOBMs, as their flux estimate includes the natural CO_2 flux component.

822 For the 2004–2014 period, the difference between the cumulative observation-based surface

823 fluxes and the ocean interior storage change of C_{ant} disappears, suggesting only a minor

824 global net outgassing of natural CO_2. However, the GOBMs (22.8 ± 2.7 Pg C dec^{-1}, Fig. 8)

825 still diagnose a 17 % weaker ocean carbon sink during the second decade compared to our

826 ocean interior estimates. The most likely explanation for this discrepancy lies in a

827 combination of three challenges that the majority of the current generation of GOBMs are

828 facing: (i) the surface to deep ocean transport of C_{ant} is rather sluggish, as these models tends

829 to underestimate the ventilation rates of the ocean interior (Terhaar et al., 2022; Fu et al.,

830 2022), (ii) the GOBMs reveal a generally lower decadal variability of the CO_2 fluxes

831 compared to observation-based estimates (Hauck et al., 2020), and (iii) the non steady-state

832 fluxes of natural CO_2 (i.e., the fluxes that are caused by climate variability) appear to be low

833 in the GOBMs. For example in the CESM-ETHZ model used in this study, the cumulative

834 flux of natural CO_2 over the 1994–2004 period amounts only to a net uptake of 0.1 Pg C dec^{-1},

835 and ranges in terms of annual fluxes from an outgassing of 0.2 Pg C yr^{-1} and an uptake of

836 0.4 Pg C yr^{-1}, which is substantially lower than the observation-based estimate determined in

837 this study.

838 Considering these three challenges of the GOBMs, the decadal offsets compared to both

839 observation-based estimates (surface and interior) could be explained as follows: During the

840 first decade, the GOBMs simulate a low anthropogenic CO_2 uptake and a low outgassing of

841 natural CO_2. The compensation of these two biases leads to an apparent agreement with the

842 surface-flux and ocean interior estimates. For the second decade, the anthropogenic CO_2

843 uptake in the GOBMs remains low, but this bias is no longer compensated for by the bias in

844 the outgassing of natural CO_2. While this interpretation of the decadal differences between

845 the three groups of estimates is internally consistent, we emphasise that most of the evaluated

846 offsets are of similar magnitude as their uncertainties. A more bottom-up assessment requires

847 the comparison of the different carbon flux components for the ensemble of GOBMs reported

848 in the GCB, an effort that is currently underway in the framework of phase 2 of the REgional

849 Carbon Cycle Assessment and Processes (RECCAP2) project (Poulter et al., 2022).

850 To put our ocean carbon sink estimates over the last two decades further into the context of

851 the global carbon cycle, we compare them with the evolution of anthropogenic carbon

852 emissions, as well as with the land and the atmospheric carbon sink extracted from the Global

853   Carbon Budget 2021 (Friedlingstein et al., 2022) for the same periods (Table 2). From this

854   comparison we derive the airborne, ocean-borne and land-borne fraction of the total

855   emissions (Table 2). Our total emission estimates comprise emissions due to the combustion

856   of fossil fuels (including the cement carbonation sink) and land use change. An important

857   aspect for the contextualisation of our ocean sink estimates is the increase of the total

858   emissions by about 25% from the first to the second decade of our analysis. In contrast, the

859   growth of the atmospheric sink for CO_2 was only about 10% higher during the second

860   decade, which is reflected in a decrease of the airborne fraction from 48 ± 4 % to 44 ± 4 %.

861   Because the emissions grew more rapidly than the atmospheric CO_2, the ocean-borne fraction

862   of C_{ant} (Table 2) decreases even more pronouncedly than the global ocean's uptake efficiency

863   β (Table 1), namely from 36 ± 4 % to 27 ± 4 % for the 1994–2004 and 2004–2014 decade,

864   respectively, which corresponds to a reduction of the uptake fraction of -9 ± 6% (or ~25% in

865   relative terms). In contrast, the land sink evolved very consistently with the total emissions

866   over the two decades, such that the land-borne fraction remained at a stable level (31 ± 6 %

867   and 30 ± 6 %). Due to the identified oceanic outgassing of natural carbon during the first but

868   not the second decade of our analysis, the net ocean sink for anthropogenic and natural

869   carbon increases in a remarkably stable manner with the total emissions. Accordingly, the

870   ocean-borne fraction of the total emissions in terms of the net oceanic CO_2 uptake remained

871   unchanged at a level of 26 ± 4 % and 26 ± 3 %. According to our assessment, the sum of all

872   three sink estimates exceeds the total emissions by about 5% during the 1994–2004 period,

873   whereas the sources and sinks of CO_2 during the 2004–2014 period match almost perfectly.

874   Although we do not identify a change in the net ocean-borne fraction of the total emissions

875   between 1994 and 2014, it is not for granted that the ocean carbon sink will remain constant

876   for the decades to come (Ridge and McKinley, 2021). DeVries et al. (2017) hypothesised that

877   a trend towards a more stratified ocean is likely to strengthen the CO_2 sink in the near future

878   by trapping natural CO_2 in the deep ocean, but further concluded that this process may

879   ultimately limit the net oceanic carbon sink, when the reduced uptake of anthropogenic CO_2

880   that continues to accumulate in the atmosphere outweighs the reduced outgassing of natural

881   carbon. Our findings demonstrate that these compensating processes are in progress and we

882   deem it of utmost importance to continue the monitoring of the ocean interior accumulation

883   of carbon to keep track of them.

884   **Table 2**: Main sources and sinks of CO_2 for the periods 1994–2004 and 2004–2014 in Pg C dec^{-1}.
885   Estimates of emissions, and the atmospheric, land and net ocean sink are based on the Global Carbon
886   Budget 2021 (Friedlingstein et al., 2022). The net ocean sink estimates represent the cumulative
887   surface fluxes based on surface-pCO_2 observations, adjusted for the outgassing of riverine carbon.
888   The oceanic sink estimates of C_{ant} are from this study, and the oceanic outgassing of natural carbon
889   was determined as the residual between the C_{ant} and the net ocean sink. The uncertainties of the
890   oceanic sink estimates follow the approach of this study, and for all other estimates apply the relative
891   uncertainties for the 2000s according to Table 6 in the GCB. Numbers in parentheses indicate the
892   airborne, land-borne, and ocean-borne fractions in % of the total emissions, with propagated
893   uncertainties from the total emissions and the sink terms.

CO_2 sources sinks	1994–2004 (Pg C yr^{-1})	2004–2014 (Pg C yr^{-1})
Total emissions	81.8 ± 7.3	100.3 ± 8.9
Fossil emissions	68.3 ± 3.5	88.2 ± 4.6
Land-use change emissions	13.5 ± 7.9	12 ± 7
Atmospheric sink **(Airborne fraction)**	39.3 ± 0.2 (48 ± 4 %)	44 ± 0.2 (44 ± 4 %)
Land sink **(Land-borne fraction)**	25 ± 4.8 (31 ± 6 %)	29.8 ± 5.7 (30 ± 6 %)
Ocean sink of C_{ant} **(Ocean-borne fraction of C_{ant})**	29.3 ± 2.5 (36 ± 4 %)	27.3 ± 2.5 (27 ± 4 %)
Inferred outgassing of natural carbon	7.9 ± 3.8	0.9 ± 2.9
Net ocean sink **(Net ocean-borne fraction)**	21.4 ± 2.8 (26 ± 4 %)	26.5 ± 1.3 (26 ± 3 %)

894   **4.4 Caveats and Recommendations**

895   Building on the quantitative uncertainty assessment of our ΔC_{ant} reconstructions (section 3.4,
896   supplement S4 and S5), we highlight in the following some caveats of our study and provide
897   recommendations on how to overcome them in future studies.

898   While all sampling periods assigned for this study are relatively well covered with
899   observations, the large changes we reconstruct in the North Atlantic between the first and
900   second period need to be viewed with caution since the number of data records that provide
901   all required variables for the eMLR(C*) analysis is very limited after ~2015. During this

902 period, a reinvigoration of the anthropogenic carbon accumulation has been reported in
903 regional studies (Raimondi et al., 2021; Fröb et al., 2018), albeit only for small subregions of
904 the whole North Atlantic. The inclusion of North Atlantic observations collected since 2015
905 into an eMLR(C*)-based ΔC_{ant} reconstruction will contribute to further improve our
906 understanding of the basin-wide C_{ant} storage changes in this highly dynamic region.

907 We further expect substantially new and improved insights from the completion of another
908 cycle of the repeat hydrography programme over the 2020s. In contrast to our two decadal
909 ΔC_{ant} reconstructions, which both build on the same data for the central sampling period
910 (2000s) and are thus not fully independent, reconstructing ocean interior trends with yet
911 another decade of observations would resolve this issue. Furthermore, future investigations
912 based on more recent data will profit from the improved data quality, in particular when
913 becoming independent from the observations of the 1990s, which tend to be less consistent
914 than the more recent measurements (Lauvset et al., 2021).

915 The continued tracking of the oceanic C_{ant} storage, e.g., by providing a global ΔC_{ant}
916 reconstruction for the 2014–2024 period, would also shed light on the very recent divergence
917 of GOBMs and surface-flux products which increased to more than 1 Pg C yr^{-1} in 2020
918 (Friedlingstein et al., 2022; Hauck et al., 2020). A burning question in this regard is whether
919 the high uptake determined by the surface flux products around 2020 can be confirmed by
920 ocean interior estimates. Scaling our C_{ant} accumulation estimates from the 2004–2014 period
921 to the 2010s according to the atmospheric CO_2 increase, we would indeed project an uptake
922 of ~32 Pg C dec^{-1}, which is very similar to the mean observation-based net surface flux over
923 the same period.

924 Another recommendation emerges from the high sensitivity of our results to the adjustments
925 we applied to a subset of the observations provided through GLODAPv2.2021. This
926 pronounced sensitivity highlights the importance of data quality and consistency for the
927 ocean interior observing system. Continued efforts to maintain and improve the quality of
928 seawater biogeochemical measurements, such as through the continued use of reference
929 materials and undertaking inter-laboratory comparisons (Bockmon and Dickson, 2015), are
930 indispensable. Furthermore, the timely submission, compilation, and harmonisation of data
931 through GLODAP appears crucial. The release of version 3 of GLODAP including a
932 complete revision of the data adjustments is anticipated in 2024. Based on our findings, we

933   suggest a critical revision of the observation from the Pacific with a particular focus on the

934   TA measurements.

935   Tightly linked to the observational data consistency is the accuracy of deep ocean ΔC_{ant}

936   reconstructions. Small biases in ΔC_{ant} can indeed exert a strong impact on the basin inventory

937   changes due to the large volume of the deep ocean. Below 1000 m, the mean ΔC_{ant}

938   reconstructed in this study is lower than 5 µmol kg^{-1} dec^{-1} across all ocean basins (Fig. 4a).

939   Despite the low ΔC_{ant} rates compared to surface waters, the ocean below 1000 m represents a

940   potentially significant contribution to the global C_{ant} inventory as it accounts for roughly 75%

941   of the total ocean volume. On a global average the content and inventory changes between

942   1000 and 3000 m carry a significant positive signal and contribute about 25% to the total

943   inventory integrated over the top 3000 m. To derive our global inventories, we have chosen

944   to account for the storage change below 3000 m (~30% of the total ocean volume) by scaling

945   the inventory with +2% according to the total C_{ant} accumulation at depth in 1994 (Sabine et

946   al., 2004). This approach is consistent with previous studies (Gruber et al., 2019) and

947   represents a compromise between neglecting deep water storage changes and potentially

948   introducing biases from integrating small and highly uncertain ΔC_{ant} below 3000m. It is

949   important to note that the general decadal trends reported in this study for the regional

950   inventories are maintained when integrating the reconstructed ΔC_{ant} across the full water

951   column, i.e., without the deep ocean scaling (data not shown). Nevertheless, we deem it

952   important that future observation-based studies explicitly include also the accumulation of

953   anthropogenic carbon in the deep ocean below 3000 m water depth, taking advantage, for

954   example, of measurements of transient tracers, such as SF$_6$ and CFCs.

955   Finally, our study revealed that fluxes of natural carbon are key to understanding the oceanic

956   response to a changing climate. The comparison of our estimates of the ocean interior

957   accumulation of anthropogenic carbon with the net surface fluxes of CO_2 allowed us to

958   distinguish a decade with presumably strong net outgassing of natural carbon (1994–2004)

959   from a decade with low net fluxes of natural carbon (2004–2014). However, our

960   quantification of the natural carbon flux as a residual quantity between two entirely

961   independent estimates remains prone to uncertainties that are in the same order of magnitude

962   as the flux itself (McNeil and Matear, 2013). As natural carbon fluxes are expected to vary

963   substantially at sub-decadal time scales, a reoccupation of selected repeat hydrography

964   sections with increased frequency or the extension of the BGC Argo programme to global

965 coverage could provide an important observational basis for future studies. Furthermore,
966 progress in the development of statistical methods to separate storage changes of natural and
967 anthropogenic carbon based on a consistent interpretation of ocean interior observations
968 alone could provide new valuable insight. The application of neural networks to reconstruct
969 ocean interior dynamics of DIC are a meaningful first step in this direction (Keppler et al.,
970 2020; Broullón et al., 2020, 2019).

5 Conclusion and Outlook

972 This study provides the first global reconstruction of the decadal evolution of the ocean
973 interior storage changes of anthropogenic carbon covering the decades 1994 to 2004 and
974 2004 to 2014. We provide uncertainty estimates for all reported estimates, including regional
975 inventories and spatial distributions of ΔC_{ant}, and decompose the uncertainties into
976 contributions from various configuration choices associated with the eMLR(C*) method.

977 We find that the oceanic sink for anthropogenic carbon remained strong during both decades
978 (29 ± 3 PgC dec^{-1} and 27 ± 3 PgC dec^{-1}, respectively). But the sink efficiency and the uptake
979 fraction of anthropogenic emissions weakened from the first to the second decade by about
980 15 and 25%, respectively. We attribute these changes to a decrease of the ocean buffer
981 capacity and a reduction in the surface ocean to deep transport, induced by changes in ocean
982 circulation (most apparent in the Atlantic) and an increase in upper ocean stratification. In
983 contrast to our findings for the accumulation of C_{ant}, observation-based estimates of the
984 surface fluxes of CO_2 indicate that the net ocean sink for anthropogenic and natural carbon
985 increased proportionally with the anthropogenic emissions. This implies that the net ocean
986 uptake fraction remained stable throughout both decades. We attribute the difference between
987 the anthropogenic and the net carbon sink to an intense (weak) outgassing of natural carbon
988 during the first (second) decades of our analysis.

989 Our results can serve as new reference points for the annual ocean sink estimates published in
990 the Global Carbon Budget and provide guidance to further develop and assess global ocean
991 biogeochemical models, which most likely underestimate the anthropogenic carbon sink.
992 Furthermore, our reconstructions of the continuing accumulation of C_{ant} can be used to infer
993 acidification trends in the ocean interior at global scale.

994   Future studies of the ocean interior storage of C_{ant} may allow us to address questions arising

995   from our analysis, including the drivers for the very recent increase in the net uptake flux as

996   determined based on surface pCO_2-observations and the question whether compensating

997   processes of the ocean carbon cycle remain effective, such as the regional shift of the

998   anthropogenic carbon storage from the North to the South Atlantic and the apparent coupling

999   between the fluxes of natural and anthropogenic carbon. Mandatory requirements to address

1000   these topics are (i) the continued and extended collection of biogeochemical ocean interior

1001   observations, i.e. the completion of a fourth cycle of the repeat hydrography programme and

1002   the expansion of the biogeochemical Argo programme to global coverage, (ii) the continued

1003   compilation of the observations into a harmonised and quality-controlled data product, and

1004   (iii) the continued improvement and further development of statistical methods, for example

1005   to separate the storage changes of anthropogenic and natural carbon.

Acknowledgments

Open Research

The anthropogenic carbon estimates reconstructed in this study are available through the Research Collection of ETH Zurich under the Creative Commons licence Attribution 4.0 International (CC BY 4.0) via the digital object identifier:

https://doi.org/10.3929/ethz-b-000590910

Upon acceptance of this manuscript for publication, a copy of this data set will be made available through NCEI's Ocean Carbon and Acidification Data System (OCADS), which is accessible under:

https://www.ncei.noaa.gov/products/ocean-carbon-acidification-data-system

All observational data sets underlying our analysis are publicly available.

The merged master file of GLODAPv2.2021 as well as the mapped climatology based on GLODAPv2 were accessed through:

www.glodap.info

The World Ocean Atlas 2018 climatology data and basin masks were accessed through:

https://www.ncei.noaa.gov/products/world-ocean-atlas

The global gridded data set of the surface ocean carbonate system (OceanSODA-ETHZ) is

1036   available under:

1037   https://doi.org/10.25921/m5wx-ja34

1038   For review purposes, the code used to preprocess the data sets, apply the eMLR(C*) method

1039   and analyse the generated output is available in these three github repositories:

1040   https://github.com/jens-daniel-mueller/emlr_obs_preprocessing

1041   https://github.com/jens-daniel-mueller/emlr_obs_v_XXX

1042   https://github.com/jens-daniel-mueller/emlr_obs_analysis

1043   The final version of the code will be made available through Zenodo via a digital object

1044   identifier upon acceptance of this manuscript for publication

References

Bittig, H. C., Steinhoff, T., Claustre, H., Fiedler, B., Williams, N. L., Sauzède, R., Körtzinger, A., and Gattuso, J.-P.: An Alternative to Static Climatologies: Robust Estimation of Open Ocean CO2 Variables and Nutrient Concentrations From T, S, and O2 Data Using Bayesian Neural Networks, Front. Mar. Sci., 5, https://doi.org/10.3389/fmars.2018.00328, 2018.

Bockmon, E. E. and Dickson, A. G.: An inter-laboratory comparison assessing the quality of seawater carbon dioxide measurements, Mar. Chem., 171, 36–43, https://doi.org/10.1016/j.marchem.2015.02.002, 2015.

Bopp, L., Lévy, M., Resplandy, L., and Sallée, J. B.: Pathways of anthropogenic carbon subduction in the global ocean, Geophys. Res. Lett., 42, 6416–6423, https://doi.org/10.1002/2015GL065073, 2015.

Broullón, D., Pérez, F. F., Velo, A., Hoppema, M., Olsen, A., Takahashi, T., Key, R. M., Tanhua, T., González-Dávila, M., Jeansson, E., Kozyr, A., and van Heuven, S. M. A. C.: A global monthly climatology of total alkalinity: a neural network approach, Earth Syst. Sci. Data, 11, 1109–1127, https://doi.org/10.5194/essd-11-1109-2019, 2019.

Broullón, D., Pérez, F. F., Velo, A., Hoppema, M., Olsen, A., Takahashi, T., Key, R. M., Tanhua, T., Santana-Casiano, J. M., and Kozyr, A.: A global monthly climatology of oceanic total dissolved inorganic carbon: a neural network approach, Earth Syst. Sci. Data, 12, 1725–1743, https://doi.org/10.5194/essd-12-1725-2020, 2020.

Carter, B. R., Feely, R. A., Wanninkhof, R., Kouketsu, S., Sonnerup, R. E., Pardo, P. C., Sabine, C. L., Johnson, G. C., Sloyan, B. M., Murata, A., Mecking, S., Tilbrook, B., Speer, K., Talley, L. D., Millero, F. J., Wijffels, S. E., Macdonald, A. M., Gruber, N., and Bullister, J. L.: Pacific Anthropogenic Carbon Between 1991 and 2017, Glob. Biogeochem. Cycles, 2018GB006154, https://doi.org/10.1029/2018GB006154, 2019.

Cheng, L., Foster, G., Hausfather, Z., Trenberth, K. E., and Abraham, J.: Improved Quantification of the Rate of Ocean Warming, J. Clim., 35, 4827–4840, https://doi.org/10.1175/JCLI-D-21-0895.1, 2022.

Clement, D. and Gruber, N.: The eMLR(C*) Method to Determine Decadal Changes in the Global Ocean Storage of Anthropogenic CO$_2$, Glob. Biogeochem. Cycles, 32, 654–679, https://doi.org/10.1002/2017GB005819, 2018.

DeVries, T. and Primeau, F.: Dynamically and Observationally Constrained Estimates of Water-Mass Distributions and Ages in the Global Ocean, J. Phys. Oceanogr., 41, 2381–2401, https://doi.org/10.1175/JPO-D-10-05011.1, 2011.

DeVries, T., Holzer, M., and Primeau, F.: Recent increase in oceanic carbon uptake driven by weaker upper-ocean overturning, Nature, 542, 215–218, https://doi.org/10.1038/nature21068, 2017.

Dickson, A. G.: Standard potential of the reaction: AgCl(s) + 12H2(g) = Ag(s) + HCl(aq), and and the standard acidity constant of the ion HSO4− in synthetic sea water from 273.15 to 318.15 K, J. Chem. Thermodyn., 22, 113–127, https://doi.org/10.1016/0021-9614(90)90074-Z, 1990.

Dickson, A. G. and Riley, J. P.: The estimation of acid dissociation constants in seawater media from potentionmetric titrations with strong base. I. The ionic product of water — Kw, Mar. Chem., 7, 89–99, https://doi.org/10.1016/0304-4203(79)90001-X, 1979.

Doney, S. C., Lima, I., Feely, R. A., Glover, D. M., Lindsay, K., Mahowald, N., Moore, J. K., and Wanninkhof, R.: Mechanisms governing interannual variability in upper-ocean inorganic carbon system and air–sea CO2 fluxes: Physical climate and atmospheric dust, Deep Sea Res. Part II Top. Stud. Oceanogr., 56, 640–655, https://doi.org/10.1016/j.dsr2.2008.12.006, 2009.

Fay, A. R., Gregor, L., Landschützer, P., McKinley, G. A., Gruber, N., Gehlen, M., Iida, Y., Laruelle, G. G., Rödenbeck, C., Roobaert, A., and Zeng, J.: SeaFlux: harmonization of air–sea CO$_2$ fluxes from surface *p*CO$_2$ data products using a standardized approach, Earth Syst. Sci. Data, 13, 4693–4710, https://doi.org/10.5194/essd-13-4693-2021, 2021.

Friedlingstein, P., Jones, M. W., O'Sullivan, M., Andrew, R. M., Bakker, D. C. E., Hauck, J., Le Quéré, C., Peters, G. P., Peters, W., Pongratz, J., Sitch, S., Canadell, J. G., Ciais, P., Jackson, R. B., Alin, S. R., Anthoni, P., Bates, N. R., Becker, M., Bellouin, N., Bopp, L., Chau, T. T. T., Chevallier, F., Chini, L. P., Cronin, M., Currie, K. I., Decharme, B., Djeutchouang, L. M., Dou, X., Evans, W., Feely, R. A., Feng, L., Gasser, T., Gilfillan, D., Gkritzalis, T., Grassi, G., Gregor, L., Gruber, N., Gürses, Ö., Harris, I., Houghton, R. A., Hurtt, G. C., Iida, Y., Ilyina, T., Luijkx, I. T., Jain, A., Jones, S. D., Kato, E., Kennedy, D., Klein Goldewijk, K., Knauer, J., Korsbakken, J. I., Körtzinger, A., Landschützer, P., Lauvset, S. K., Lefèvre, N., Lienert, S., Liu, J., Marland, G., McGuire, P. C., Melton, J. R., Munro, D. R., Nabel, J. E. M. S., Nakaoka, S.-I., Niwa, Y., Ono, T., Pierrot, D., Poulter, B., Rehder, G., Resplandy, L., Robertson, E., Rödenbeck, C., Rosan, T. M., Schwinger, J., Schwingshackl, C., Séférian, R., Sutton, A. J., Sweeney, C., Tanhua, T., Tans, P. P., Tian, H., Tilbrook, B., Tubiello, F., van der Werf, G. R., Vuichard, N., Wada, C., Wanninkhof, R., Watson, A. J., Willis, D., Wiltshire, A. J., Yuan, W., Yue, C., Yue, X., Zaehle, S., and Zeng, J.: Global Carbon Budget 2021, Earth Syst. Sci. Data, 14, 1917–2005, https://doi.org/10.5194/essd-14-1917-2022, 2022.

Fröb, F., Olsen, A., Våge, K., Moore, G. W. K., Yashayaev, I., Jeansson, E., and Rajasakaren, B.: Irminger Sea deep convection injects oxygen and anthropogenic carbon to the ocean interior, Nat. Commun., 7, 13244, https://doi.org/10.1038/ncomms13244, 2016.

Fröb, F., Olsen, A., Pérez, F. F., García-Ibáñez, M. I., Jeansson, E., Omar, A., and Lauvset, S. K.: Inorganic carbon and water masses in the Irminger Sea since 1991, Biogeosciences, 15, 51–72, https://doi.org/10.5194/bg-15-51-2018, 2018.

Fu, W., Moore, J. K., Primeau, F., Collier, N., Ogunro, O. O., Hoffman, F. M., and Randerson, J. T.: Evaluation of ocean biogeochemistry and carbon cycling in CMIP earth system models with the International Ocean Model Benchmarking (IOMB) software system, J. Geophys. Res. Oceans, n/a, e2022JC018965, https://doi.org/10.1029/2022JC018965, 2022.

Gammon, R. H., Cline, J., and Wisegarver, D.: Chlorofluoromethanes in the northeast Pacific Ocean: Measured vertical distributions and application as transient tracers of upper ocean mixing, J. Geophys. Res. Oceans, 87, 9441–9454, https://doi.org/10.1029/JC087iC12p09441, 1982.

Gao, H., Cai, W.-J., Jin, M., Dong, C., and Timmerman, A. H. V.: Ocean Ventilation Controls the Contrasting Anthropogenic CO2 Uptake Rates Between the Western and Eastern South Atlantic Ocean Basins, Glob. Biogeochem. Cycles, 36, e2021GB007265, https://doi.org/10.1029/2021GB007265, 2022.

Gattuso, J.-P., Epitalon, J.-M., Lavigne, H., and Orr, J.: seacarb: Seawater Carbonate Chemistry, 2021.

Graham, F. S. and McDougall, T. J.: Quantifying the Nonconservative Production of Conservative Temperature, Potential Temperature, and Entropy, J. Phys. Oceanogr., 43, 838–862, https://doi.org/10.1175/JPO-D-11-0188.1, 2013.

Gregor, L. and Gruber, N.: OceanSODA-ETHZ: a global gridded data set of the surface ocean carbonate system for seasonal to decadal studies of ocean acidification, Earth Syst. Sci. Data, 13, 777–808, https://doi.org/10.5194/essd-13-777-2021, 2021.

Gruber, N., Sarmiento, J. L., and Stocker, T. F.: An improved method for detecting anthropogenic CO2 in the oceans, Glob. Biogeochem. Cycles, 10, 809–837, https://doi.org/10.1029/96GB01608, 1996.

Gruber, N., Clement, D., Carter, B. R., Feely, R. A., van Heuven, S., Hoppema, M., Ishii, M., Key, R. M., Kozyr, A., Lauvset, S. K., Lo Monaco, C., Mathis, J. T., Murata, A., Olsen, A., Perez, F. F., Sabine, C. L., Tanhua, T., and Wanninkhof, R.: The oceanic sink for anthropogenic CO2 from 1994 to 2007, Science, 363, 1193–1199, https://doi.org/10.1126/science.aau5153, 2019.

Hauck, J., Zeising, M., Le Quéré, C., Gruber, N., Bakker, D. C. E., Bopp, L., Chau, T. T. T., Gürses, Ö., Ilyina, T., Landschützer, P., Lenton, A., Resplandy, L., Rödenbeck, C., Schwinger, J., and Séférian, R.: Consistency and Challenges in the Ocean Carbon Sink Estimate for the Global Carbon Budget, Front. Mar. Sci., 7, https://doi.org/10.3389/fmars.2020.571720, 2020.

Holliday, N. P., Bersch, M., Berx, B., Chafik, L., Cunningham, S., Florindo-López, C., Hátún, H., Johns, W., Josey, S. A., Larsen, K. M. H., Mulet, S., Oltmanns, M., Reverdin, G., Rossby, T., Thierry, V., Valdimarsson, H., and Yashayaev, I.: Ocean circulation causes the largest freshening event for 120 years in eastern subpolar North Atlantic, Nat. Commun., 11, 585, https://doi.org/10.1038/s41467-020-14474-y, 2020.

1140   IPCC: IPCC Special Report on the Ocean and Cryosphere in a Changing Climate [H.-O. Pörtner, D.C. Roberts,
1141   V. Masson-Delmotte, P. Zhai, M. Tignor, E. Poloczanska, K. Mintenbeck, A. Alegría, M. Nicolai, A. Okem, J.
1142   Petzold, B. Rama, N.M. Weyer (eds.)], Cambridge University Press, https://doi.org/10.1017/9781009157964,
1143   2019.

1144   Jackson, L. C., Dubois, C., Forget, G., Haines, K., Harrison, M., Iovino, D., Köhl, A., Mignac, D., Masina, S.,
1145   Peterson, K. A., Piecuch, C. G., Roberts, C. D., Robson, J., Storto, A., Toyoda, T., Valdivieso, M., Wilson, C.,
1146   Wang, Y., and Zuo, H.: The Mean State and Variability of the North Atlantic Circulation: A Perspective From
1147   Ocean Reanalyses, J. Geophys. Res. Oceans, 124, 9141–9170, https://doi.org/10.1029/2019JC015210, 2019.

1148   Jackson, L. C., Biastoch, A., Buckley, M. W., Desbruyères, D. G., Frajka-Williams, E., Moat, B., and Robson,
1149   J.: The evolution of the North Atlantic Meridional Overturning Circulation since 1980, Nat. Rev. Earth
1150   Environ., 1–14, https://doi.org/10.1038/s43017-022-00263-2, 2022.

1151   Jacobson, A. R., Fletcher, S. E. M., Gruber, N., Sarmiento, J. L., and Gloor, M.: A joint atmosphere-ocean
1152   inversion for surface fluxes of carbon dioxide: 2. Regional results, Glob. Biogeochem. Cycles, 21,
1153   https://doi.org/10.1029/2006GB002703, 2007.

1154   Jiang, L.-Q., Carter, B. R., Feely, R. A., Lauvset, S. K., and Olsen, A.: Surface ocean pH and buffer capacity:
1155   past, present and future, Sci. Rep., 9, 18624, https://doi.org/10.1038/s41598-019-55039-4, 2019.

1156   Keppler, L., Landschützer, P., Gruber, N., Lauvset, S. K., and Stemmler, I.: Seasonal Carbon Dynamics in the
1157   Near-Global Ocean, Glob. Biogeochem. Cycles, 34, e2020GB006571, https://doi.org/10.1029/2020GB006571,
1158   2020.

1159   Key, R. M., Kozyr, A., Sabine, C. L., Lee, K., Wanninkhof, R., Bullister, J. L., Feely, R. A., Millero, F. J.,
1160   Mordy, C., and Peng, T.-H.: A global ocean carbon climatology: Results from Global Data Analysis Project
1161   (GLODAP), Glob. Biogeochem. Cycles, 18, https://doi.org/10.1029/2004GB002247, 2004.

1162   Khatiwala, S., Primeau, F., and Hall, T.: Reconstruction of the history of anthropogenic CO 2 concentrations in
1163   the ocean, Nature, 462, 346–349, https://doi.org/10.1038/nature08526, 2009.

1164   Khatiwala, S., Tanhua, T., Mikaloff Fletcher, S., Gerber, M., Doney, S. C., Graven, H. D., Gruber, N.,
1165   McKinley, G. A., Murata, A., Ríos, A. F., and Sabine, C. L.: Global ocean storage of anthropogenic carbon,
1166   Biogeosciences, 10, 2169–2191, https://doi.org/10.5194/bg-10-2169-2013, 2013.

1167   Landschützer, P., Gruber, N., Haumann, F. A., Rödenbeck, C., Bakker, D. C. E., van Heuven, S., Hoppema, M.,
1168   Metzl, N., Sweeney, C., Takahashi, T., Tilbrook, B., and Wanninkhof, R.: The reinvigoration of the Southern
1169   Ocean carbon sink, Science, 349, 1221–1224, https://doi.org/10.1126/science.aab2620, 2015.

1170   Landschützer, P., Gruber, N., and Bakker, D. C. E.: Decadal variations and trends of the global ocean carbon
1171   sink, Glob. Biogeochem. Cycles, 30, 1396–1417, https://doi.org/10.1002/2015GB005359, 2016.

1172   Latif, M., Sun, J., Visbeck, M., and Hadi Bordbar, M.: Natural variability has dominated Atlantic Meridional
1173   Overturning Circulation since 1900, Nat. Clim. Change, 1–6, https://doi.org/10.1038/s41558-022-01342-4,
1174   2022.

1175   Lauvset, S. K., Key, R. M., Olsen, A., van Heuven, S., Velo, A., Lin, X., Schirnick, C., Kozyr, A., Tanhua, T.,
1176   Hoppema, M., Jutterström, S., Steinfeldt, R., Jeansson, E., Ishii, M., Perez, F. F., Suzuki, T., and Watelet, S.: A
1177   new global interior ocean mapped climatology: the 1∘ × 1∘ GLODAP version 2, 16, 2016.

1178   Lauvset, S. K., Lange, N., Tanhua, T., Bittig, H. C., Olsen, A., Kozyr, A., Álvarez, M., Becker, S., Brown, P. J.,
1179   Carter, B. R., Cotrim da Cunha, L., Feely, R. A., van Heuven, S., Hoppema, M., Ishii, M., Jeansson, E.,
1180   Jutterström, S., Jones, S. D., Karlsen, M. K., Lo Monaco, C., Michaelis, P., Murata, A., Pérez, F. F., Pfeil, B.,
1181   Schirnick, C., Steinfeldt, R., Suzuki, T., Tilbrook, B., Velo, A., Wanninkhof, R., Woosley, R. J., and Key, R.
1182   M.: An updated version of the global interior ocean biogeochemical data product, GLODAPv2.2021, Earth Syst.
1183   Sci. Data, 13, 5565–5589, https://doi.org/10.5194/essd-13-5565-2021, 2021.

1184   Lauvset, S. K., Lange, N., Tanhua, T., Bittig, H. C., Olsen, A., Kozyr, A., Alin, S., Álvarez, M., Azetsu-Scott,
1185   K., Barbero, L., Becker, S., Brown, P. J., Carter, B. R., da Cunha, L. C., Feely, R. A., Hoppema, M.,
1186   Humphreys, M. P., Ishii, M., Jeansson, E., Jiang, L.-Q., Jones, S. D., Lo Monaco, C., Murata, A., Müller, J. D.,
1187   Pérez, F. F., Pfeil, B., Schirnick, C., Steinfeldt, R., Suzuki, T., Tilbrook, B., Ulfsbo, A., Velo, A., Woosley, R.

J., and Key, R. M.: GLODAPv2.2022: the latest version of the global interior ocean biogeochemical data product, Earth Syst. Sci. Data, 14, 5543–5572, https://doi.org/10.5194/essd-14-5543-2022, 2022.

Le Quéré, C., Rödenbeck, C., Buitenhuis, E. T., Conway, T. J., Langenfelds, R., Gomez, A., Labuschagne, C., Ramonet, M., Nakazawa, T., Metzl, N., Gillett, N., and Heimann, M.: Saturation of the Southern Ocean CO2 Sink Due to Recent Climate Change, Science, 316, 1735–1738, https://doi.org/10.1126/science.1136188, 2007.

Li, G., Cheng, L., Zhu, J., Trenberth, K. E., Mann, M. E., and Abraham, J. P.: Increasing ocean stratification over the past half-century, Nat. Clim. Change, 1–8, https://doi.org/10.1038/s41558-020-00918-2, 2020.

Locarnini, R., Mishonov, A., Baranova, O., Boyer, T., Zweng, M., Garcia, H., Reagan, J., Seidov, D., Weathers, K., Paver, C., Smolyar, I., and Locarnini, R.: World Ocean Atlas 2018, Volume 1: Temperature, 2019.

Lovenduski, N. S., Gruber, N., and Doney, S. C.: Toward a mechanistic understanding of the decadal trends in the Southern Ocean carbon sink, Glob. Biogeochem. Cycles, 22, https://doi.org/10.1029/2007GB003139, 2008.

Lueker, T. J., Dickson, A. G., and Keeling, C. D.: Ocean pCO2 calculated from dissolved inorganic carbon, alkalinity, and equations for K1 and K2: validation based on laboratory measurements of CO2 in gas and seawater at equilibrium, Mar. Chem., 70, 105–119, https://doi.org/10.1016/S0304-4203(00)00022-0, 2000.

McNeil, B. I. and Matear, R. J.: The non-steady state oceanic CO_2 signal: its importance, magnitude and a novel way to detect it, Biogeosciences, 10, 2219–2228, https://doi.org/10.5194/bg-10-2219-2013, 2013.

McNeil, B. I., Matear, R. J., Key, R. M., Bullister, J. L., and Sarmiento, J. L.: Anthropogenic CO2 Uptake by the Ocean Based on the Global Chlorofluorocarbon Data Set, Science, 299, 235–239, https://doi.org/10.1126/science.1077429, 2003.

Olsen, A., Omar, A. M., Jeansson, E., Anderson, L. G., and Bellerby, R. G. J.: Nordic seas transit time distributions and anthropogenic CO2, J. Geophys. Res. Oceans, 115, https://doi.org/10.1029/2009JC005488, 2010.

Olsen, A., Key, R. M., van Heuven, S., Lauvset, S. K., Velo, A., Lin, X., Schirnick, C., Kozyr, A., Tanhua, T., Hoppema, M., Jutterström, S., Steinfeldt, R., Jeansson, E., Ishii, M., Pérez, F. F., and Suzuki, T.: The Global Ocean Data Analysis Project version 2 (GLODAPv2) – an internallyconsistent data product for the world ocean, Earth Syst. Sci. Data, 8, 297–323, https://doi.org/10.5194/essd-8-297-2016, 2016.

Palmiéri, J., Orr, J. C., Dutay, J.-C., Béranger, K., Schneider, A., Beuvier, J., and Somot, S.: Simulated anthropogenic CO_2 storage and acidification of the Mediterranean Sea, Biogeosciences, 12, 781–802, https://doi.org/10.5194/bg-12-781-2015, 2015.

Park, G.-H., Lee, K., Tishchenko, P., Min, D.-H., Warner, M. J., Talley, L. D., Kang, D.-J., and Kim, K.-R.: Large accumulation of anthropogenic CO2 in the East (Japan) Sea and its significant impact on carbonate chemistry, Glob. Biogeochem. Cycles, 20, https://doi.org/10.1029/2005GB002676, 2006.

Patara, L., Böning, C. W., and Tanhua, T.: Multidecadal Changes in Southern Ocean Ventilation since the 1960s Driven by Wind and Buoyancy Forcing, J. Clim., 34, 1485–1502, https://doi.org/10.1175/JCLI-D-19-0947.1, 2021.

Perez, F. F. and Fraga, F.: Association constant of fluoride and hydrogen ions in seawater, Mar. Chem., 21, 161–168, https://doi.org/10.1016/0304-4203(87)90036-3, 1987.

Pérez, F. F., Vázquez-Rodríguez, M., Mercier, H., Velo, A., Lherminier, P., and Ríos, A. F.: Trends of anthropogenic CO_2 storage in North Atlantic water masses, Biogeosciences, 7, 1789–1807, https://doi.org/10.5194/bg-7-1789-2010, 2010.

Pérez, F. F., Mercier, H., Vázquez-Rodríguez, M., Lherminier, P., Velo, A., Pardo, P. C., Rosón, G., and Ríos, A. F.: Atlantic Ocean CO2 uptake reduced by weakening of the meridional overturning circulation, Nat. Geosci., 6, 146–152, https://doi.org/10.1038/ngeo1680, 2013.

Poulter, B., Bastos, A., Canadell, J., Ciais, P., Gruber, N., Hauck, J., Jackson, R., Ishii, M., Müller, Jens Daniel, J., Patra, P., and Tian, H.: Inventorying Earth's Land and Ocean Greenhouse Gases, Eos, 103, https://doi.org/10.1029/2022eo179084, 2022.

1234 Raimondi, L., Tanhua, T., Azetsu-Scott, K., Yashayaev, I., and Wallace, D. w. r.: A 30 -Year Time Series of
1235 Transient Tracer-Based Estimates of Anthropogenic Carbon in the Central Labrador Sea, J. Geophys. Res.
1236 Oceans, 126, e2020JC017092, https://doi.org/10.1029/2020JC017092, 2021.

1237 Resplandy, L., Keeling, R. F., Rödenbeck, C., Stephens, B. B., Khatiwala, S., Rodgers, K. B., Long, M. C.,
1238 Bopp, L., and Tans, P. P.: Revision of global carbon fluxes based on a reassessment of oceanic and riverine
1239 carbon transport, Nat. Geosci., 11, 504–509, https://doi.org/10.1038/s41561-018-0151-3, 2018.

1240 Ridge, S. M. and McKinley, G. A.: Ocean carbon uptake under aggressive emission mitigation, Biogeosciences,
1241 18, 2711–2725, https://doi.org/10.5194/bg-18-2711-2021, 2021.

1242 Sabine, C. L., Feely, R. A., Gruber, N., Key, R. M., Lee, K., Bullister, J. L., Wanninkhof, R., Wong, C. S.,
1243 Wallace, D. W. R., Tilbrook, B., Millero, F. J., Peng, T.-H., Kozyr, A., Ono, T., and Rios, A. F.: The Oceanic
1244 Sink for Anthropogenic CO2, Science, 305, 367–371, https://doi.org/10.1126/science.1097403, 2004.

1245 Sallée, J.-B., Pellichero, V., Akhoudas, C., Pauthenet, E., Vignes, L., Schmidtko, S., Garabato, A. N.,
1246 Sutherland, P., and Kuusela, M.: Summertime increases in upper-ocean stratification and mixed-layer depth,
1247 Nature, 591, 592–598, https://doi.org/10.1038/s41586-021-03303-x, 2021.

1248 Shi, J.-R., Talley, L. D., Xie, S.-P., Peng, Q., and Liu, W.: Ocean warming and accelerating Southern Ocean
1249 zonal flow, Nat. Clim. Change, 1–8, https://doi.org/10.1038/s41558-021-01212-5, 2021.

1250 Sloyan, B. M., Wanninkhof, R., Kramp, M., Johnson, G. C., Talley, L. D., Tanhua, T., McDonagh, E., Cusack,
1251 C., O'Rourke, E., McGovern, E., Katsumata, K., Diggs, S., Hummon, J., Ishii, M., Azetsu-Scott, K., Boss, E.,
1252 Ansorge, I., Perez, F. F., Mercier, H., Williams, M. J. M., Anderson, L., Lee, J. H., Murata, A., Kouketsu, S.,
1253 Jeansson, E., Hoppema, M., and Campos, E.: The Global Ocean Ship-Based Hydrographic Investigations
1254 Program (GO-SHIP): A Platform for Integrated Multidisciplinary Ocean Science, Front. Mar. Sci., 6,
1255 https://doi.org/10.3389/fmars.2019.00445, 2019.

1256 Talley, L. d., Feely, R. a., Sloyan, B. m., Wanninkhof, R., Baringer, M. o., Bullister, J. l., Carlson, C. a., Doney,
1257 S. c., Fine, R. a., Firing, E., Gruber, N., Hansell, D. a., Ishii, M., Johnson, G. c., Katsumata, K., Key, R. m.,
1258 Kramp, M., Langdon, C., Macdonald, A. m., Mathis, J. t., McDonagh, E. l., Mecking, S., Millero, F. j., Mordy,
1259 C. w., Nakano, T., Sabine, C. l., Smethie, W. m., Swift, J. h., Tanhua, T., Thurnherr, A. m., Warner, M. j., and
1260 Zhang, J.-Z.: Changes in Ocean Heat, Carbon Content, and Ventilation: A Review of the First Decade of GO-
1261 SHIP Global Repeat Hydrography, Annu. Rev. Mar. Sci., 8, 185–215, https://doi.org/10.1146/annurev-marine-
1262 052915-100829, 2016.

1263 Tanhua, T., Jones, E. P., Jeansson, E., Jutterström, S., Smethie, W. M., Wallace, D. W. R., and Anderson, L. G.:
1264 Ventilation of the Arctic Ocean: Mean ages and inventories of anthropogenic CO2 and CFC-11, J. Geophys.
1265 Res. Oceans, 114, https://doi.org/10.1029/2008JC004868, 2009.

1266 Terhaar, J., Frölicher, T. L., and Joos, F.: Observation-constrained estimates of the global ocean carbon sink
1267 from Earth system models, Biogeosciences, 19, 4431–4457, https://doi.org/10.5194/bg-19-4431-2022, 2022.

1268 Wallace, D. W. R.: Monitoring Global Ocean Carbon Inventories, 1995.

1269 Wanninkhof, R., Doney, S. C., Bullister, J. L., Levine, N. M., Warner, M., and Gruber, N.: Detecting
1270 anthropogenic CO2 changes in the interior Atlantic Ocean between 1989 and 2005, J. Geophys. Res. Oceans,
1271 115, https://doi.org/10.1029/2010JC006251, 2010.

1272 Watson, A. J., Schuster, U., Shutler, J. D., Holding, T., Ashton, I. G. C., Landschützer, P., Woolf, D. K., and
1273 Goddijn-Murphy, L.: Revised estimates of ocean-atmosphere CO2 flux are consistent with ocean carbon
1274 inventory, Nat. Commun., 11, 4422, https://doi.org/10.1038/s41467-020-18203-3, 2020.

1275 Weiss, R. F.: The solubility of nitrogen, oxygen and argon in water and seawater, Deep Sea Res. Oceanogr.
1276 Abstr., 17, 721–735, https://doi.org/10.1016/0011-7471(70)90037-9, 1970.

1277 Woosley, R. J., Millero, F. J., and Wanninkhof, R.: Rapid anthropogenic changes in CO2 and pH in the Atlantic
1278 Ocean: 2003–2014, Glob. Biogeochem. Cycles, 30, 70–90, https://doi.org/10.1002/2015GB005248, 2016.

1279 Young, I. R. and Ribal, A.: Multiplatform evaluation of global trends in wind speed and wave height, Science,
1280 364, 548–552, https://doi.org/10.1126/science.aav9527, 2019.

1281   Zweng, M. M., Reagan, J., Seidov, D., Boyer, T., Locarnini, R., Garcia, H., Mishonov, A., Baranova, O. K.,
1282   Paver, C., and Smolyar, I.: WORLD OCEAN ATLAS 2018 Volume 2: Salinity, 2019.